POLITECNICO DI TORINO

Master's Degree in Aerospace Engineering



Master's Degree Thesis

Station-Keeping Optimization in Low Earth Orbit under Low-Thrust Propulsion with Eclipse Constraints

Supervisors

Candidate

Prof. Manuela BATTIPEDE

Alessandro ZORGNIOTTI

Dr. Luigi MASCOLO

October 2025

Abstract

This thesis investigates the optimal control of low-thrust satellites operating in Sun-synchronous orbits (SSOs), with particular attention to the effects of atmospheric drag and eclipse constraints. The work addresses the challenge of maintaining orbital stability when thrust application is limited by environmental conditions, such as power unavailability during eclipse and the continuous loss of orbital energy due to drag.

The problem is formulated as an optimal control problem and solved using Pontryagin's Maximum Principle, leading to a boundary value problem addressed through an indirect shooting method. Atmospheric density is modeled using the NRLMSISE-00 model, while eclipse prediction is based on a cylindrical shadow formulation combined with ephemerides data obtained through SPICE.

A modular Python software environment, originally based on the *Oculus* framework, has been extended to include atmospheric drag and eclipse modeling. A graphical user interface supports scenario configuration and visualization of the optimized solutions.

The developed framework is applied to three representative scenarios: an ideal case with only two-body dynamics and continuous thrust, a case including atmospheric drag, and a full model incorporating both drag and eclipse constraints. The progressive comparison of these cases illustrates the impact of environmental effects on thrust scheduling and orbital maintenance strategies.

Acknowledgements

I would like to express my deepest gratitude to Professor Luigi Mascolo, whose guidance, expertise, and availability were fundamental throughout the development of this thesis. His scientific rigor and passion for astrodynamics have been a true source of inspiration.

I would also like to thank Professor Manuela Battipede for her support and for providing a valuable academic framework for this work.

A special thank you goes to my family, whose constant encouragement and unconditional support have accompanied me throughout my academic journey.

To my girlfriend, for her patience, love, and understanding during the most intense phases of this work.

Finally, I am grateful to my friends, who have been a source of relief, motivation, and balance in and out of the academic context.

Table of Contents

Li	st of	Figures	VI
A	crony	yms	VIII
1	Intr	roduction	1
	1.1	Background and Motivation	1
	1.2	Literature and Historical Context	2
	1.3	Objective of this Thesis	4
	1.4	Dissertation Overview	5
2	Dyr	namic Models	6
	2.1	Introduction to Orbital Dynamics	6
	2.2	Reference Frames and Transformations	7
	2.3	The Two-Body Problem	13
	2.4	Perturbation Models	16
		2.4.1 Introduction to Perturbations	16
		2.4.2 Zonal Harmonics and the J_2 Perturbation	17
		2.4.3 Application to Sun-Synchronous Orbits	18
		2.4.4 Atmospheric Drag	19
		2.4.5 Solar Radiation Pressure	19
3	Opt	cimal control theory	21
	3.1	Introduction and Problem Definition	21
	3.2	General Formulation of an Optimal Control Problem	22
	3.3	Pontryagin Minimum Principle	24
		3.3.1 Physical and mathematical interpretation of costates	26
	3.4	Optimal Control Law	27
	3.5	Boundary Conditions and Constraints	29
	3.6	Numerical Solution Approach	31

	_				
4	Dyı	namic Modeling and Optimal Control Formulation	34		
	4.1	Problem Setup and Modeling Framework	34		
	4.2	Dynamical Model Formulation	35		
	4.3	Atmospheric Drag Modeling	37		
	4.4	Eclipse Modeling and Sun Visibility	40		
	4.5	Optimal Control Problem Formulation for the LEO Scenario	42		
	4.6	Numerical Implementation	45		
	4.7	Graphical User Interface	48		
5	Res	ult and Analysis	49		
	5.1	Simulation Setup and Parameters	49		
	5.2	Baseline Case – Ideal Dynamics (No Perturbations)	51		
	5.3	Dynamics with Atmospheric Drag Only	53		
	5.4	Full Model: Drag and Eclipse Constraint	54		
6	Cor	nclusions and Future Work	57		
Bi	Bibliography 60				

List of Figures

2.1	Example of SSO	7
2.2	ECI, Perifocal, NEZ	8
2.3	ECI	8
2.4	ECEF	9
2.5	NEZ	10
2.6	Two Body Problem scheme	13
2.7	Condition for Sun-synchronicity: the J_2 -induced regression of the	
	node matches the apparent motion of the Sun	18
4.1	Comparison between the exponential model, tabulated-interpolated	
	MSISE-00, and the reference MSISE-00 output	39
4.2	Relative error density	40
5.1	Baseline case: Variable evolution under low thrust in a two-body	
	environment	52
5.2	Time evolution of the state variables for the drag-included scenario.	54
5.3	Graphical user interface view of the full-model case	55
5.4	Time evolution of the state variables for the full-model case	56

Acronyms

CR3BP

Circular Restricted Three-Body Problem

GST

Greenwich Sidereal Time

ECEF

Earth-Centered Earth-Fixed

ECI

Earth-Centered Inertial

LEO

Low Earth Orbit

NEZ

North-East-Zenith

PMP

Pontryagin's Maximum Principle

RAAN

Right Ascension of Ascending Node

R3BP

Restricted three-body problem

SSOs

Sun Syncronous Orbits

TPBVP

Two-Point Boundary Value Problem

2BP

Two-Body problem

Chapter 1

Introduction

1.1 Background and Motivation

The modern landscape of space missions is increasingly shaped by the need for autonomy, efficiency, and long-term operability. As satellites are tasked with more complex maneuvers and tighter mission constraints, trajectory optimization has become a central element of mission design and control. Among the technological advancements driving this evolution, low-thrust propulsion systems — such as Hall-effect thrusters and ion engines — have fundamentally transformed orbit control. These systems provide continuous and finely tunable thrust, offering substantial gains in fuel efficiency and enabling extended mission lifetimes, progressive orbit raising, and precise station-keeping. However, their effective use demands sophisticated mathematical tools capable of handling long-duration maneuvers in nonlinear and time-varying dynamical environments.

At the same time, real missions are constrained by physical and operational limitations that strongly influence thrust scheduling. Among the most critical are power availability and environmental effects. Solar-powered spacecraft must suspend thrust during eclipse phases, when they receive no sunlight, either to conserve energy or to avoid overloading their power subsystems. This introduces time-dependent discontinuities in the control input, forcing the guidance law to adapt to periods when thrust cannot be applied. Similarly, atmospheric drag continuously removes orbital energy and causes secular decay of the semi-major axis, requiring periodic reboost maneuvers to maintain the desired orbit. These effects significantly complicate the trajectory optimization problem and render traditional impulsive or analytical approaches inadequate.

Optimal control theory provides a powerful framework to address such challenges. By formulating the problem as a constrained optimization problem over a dynamical system, it is possible to derive control laws that minimise fuel consumption or mission time while respecting physical constraints such as thrust availability, power limitations, or boundary conditions on orbit geometry. Both direct (discretization-based) and indirect (Pontryagin's Maximum Principle) approaches have been applied to low-thrust orbit transfers, station-keeping, rendezvous, and interplanetary missions. These methods allow the inclusion of nonlinear dynamics, time-varying constraints, and environmental perturbations in a unified framework.

The accuracy and tractability of such methods, however, depend critically on the fidelity of the underlying dynamical model. While the classical two-body problem remains a useful first approximation, it is insufficient for precise long-term analysis. Perturbations due to Earth's oblateness, atmospheric drag, solar radiation pressure, and third-body attractions become relevant for orbit propagation and control, especially in low Earth orbit. Moreover, the choice of coordinate system affects both the physical interpretation and the numerical properties of the problem. Spherical coordinates, for instance, are often advantageous for modeling altitude variations, ground-track evolution, and eclipse geometry.

This thesis is motivated by the growing need for accurate and efficient tools to support orbit control in realistic operational conditions. The focus is on spacecraft operating in Low Earth Orbit (LEO), and in particular on Sun-synchronous orbits (SSOs), which are widely used for Earth observation and scientific missions. These orbits are especially sensitive to perturbations and depend on continuous solar illumination for power generation, making them an ideal context in which to study the interplay between atmospheric drag, eclipse constraints, and optimal thrust scheduling.

The representative problem addressed in this work is the station-keeping of a satellite in a Sun-synchronous orbit, with a discontinuous thrust profile imposed by eclipse phases. This scenario encapsulates many of the challenges encountered in real missions and provides a relevant case study for developing and validating optimal control strategies under realistic physical constraints.

1.2 Literature and Historical Context

The study of orbital mechanics dates back to the foundational works of Johannes Kepler and Isaac Newton, whose laws provided the first predictive models for planetary motion. Newton's law of universal gravitation, combined with his second law of motion, laid the groundwork for what would later be formalized as the two-body problem (2BP). This analytical solution describes the motion of a satellite around a central mass under the assumption of spherical symmetry and no external perturbations. While elegant and insightful, the two-body problem alone cannot capture the full complexity of real-world orbital dynamics.

To address more realistic scenarios, extended models have been developed over

the centuries. These include the restricted three-body problem (R3BP), which incorporates the gravitational influence of a secondary body (e.g., the Moon or the Sun), and high-fidelity models accounting for non-spherical gravity fields, atmospheric drag, solar radiation pressure, and third-body perturbations. The development of such models has paralleled the evolution of space missions — from early satellite deployments to modern interplanetary exploration — where higher accuracy and long-term reliability are paramount.

The optimization of spacecraft trajectories has also undergone significant evolution. In the early space era, trajectory design was largely based on impulsive maneuvers and patched conic approximations. These approaches, while computationally simple, relied heavily on simplifying assumptions and pre-defined maneuver structures. With the advent of more advanced computing and the emergence of low-thrust propulsion systems, new challenges arose: continuous thrusting, long-duration maneuvers, and nonlinear dynamics required more sophisticated techniques.

This led to the adoption of optimal control theory as a systematic framework for trajectory optimization. The indirect approach, grounded in Pontryagin's Maximum Principle (PMP), enables the derivation of necessary conditions for optimality in a dynamical system. This approach has been successfully applied to a wide range of problems, including fuel-optimal orbit transfers, deorbiting, rendezvous, and attitude reorientation. However, it often results in boundary value problems that can be sensitive to initial guesses and challenging to solve numerically.

To overcome these difficulties, direct methods — such as direct transcription and collocation — have been developed. These techniques discretize the control problem into a nonlinear programming problem, making them robust and well-suited for problems with complex constraints or limited regularity. Numerous software tools and solvers, such as GPOPS-II, CasADi, and DIDO, have been developed to implement these techniques efficiently, and have been employed in both academic and industrial mission design.

In the context of low Earth orbit (LEO) operations, especially for missions that rely on solar power and require precise orbit maintenance (such as Earth observation or remote sensing), optimal control theory offers a natural way to incorporate thrust limitations, eclipse periods, and perturbation effects into trajectory planning. Several recent studies have investigated eclipse-aware thrust scheduling, J2-influenced orbit control, and minimum-fuel strategies for Sun-synchronous orbit maintenance.

This thesis builds upon this growing body of literature by focusing on a specific yet representative problem: station-keeping in a Sun-synchronous orbit with the additional constraint of no-thrust during eclipse. It combines classical orbital theory, modern control techniques, and high-fidelity dynamical modeling in a unified approach aimed at both theoretical understanding and practical application.

1.3 Objective of this Thesis

The primary objective of this thesis is to investigate the problem of optimal orbit maintenance for spacecraft operating in Sun-synchronous orbits (SSOs) under realistic environmental and operational constraints, with particular emphasis on the combined effects of atmospheric drag and eclipse. The focus is on designing thrust strategies that minimise propellant consumption while ensuring orbital stability and mission continuity despite power limitations and perturbing forces.

A key operational challenge for solar-powered satellites is the inability to apply thrust during eclipse phases, when the spacecraft is temporarily deprived of solar power. This constraint imposes discontinuities in the control input and introduces additional complexity into the trajectory optimisation process. Furthermore, atmospheric drag continuously reduces orbital energy, leading to secular decay of altitude and requiring regular station-keeping manoeuvres. Together, these effects make the problem time-dependent, state-constrained, and highly nonlinear.

To address this challenge, the station-keeping problem is formulated as an optimal control problem and solved using the indirect approach based on Pontryagin's Minimum Principle. The spacecraft dynamics are described by a modified two-body model expressed in spherical coordinates (r, θ, ϕ) and coupled with a local NEZ frame for the velocity components. The model includes central gravity, atmospheric drag computed using the NRLMSISE-00 density model, and an eclipse constraint derived from the cylindrical shadow geometry and ephemerides obtained via SPICE.

A modular Python tool with a graphical user interface — originally based on the *Oculus* framework [1] and extended in this work — was developed to implement the dynamical model and solve the optimal control problem. The thrust law is modelled as piecewise-constant, taking the value $T_{\rm max}$ in illuminated regions and zero during eclipse.

The main contributions of this thesis can be summarised as follows:

- Development of a high-fidelity dynamical model incorporating gravitational forces, atmospheric drag, and eclipse constraints in spherical coordinates.
- Formulation of the optimal control problem with discontinuous thrust availability and solution using an indirect shooting method.
- Extension of the existing *Oculus* tool with new modules for atmospheric drag computation and eclipse detection, enabling realistic mission simulation.
- Numerical analysis of three representative scenarios (ideal dynamics, drag only, and drag with eclipse) to assess how environmental effects influence optimal control structure, thrust distribution, and mission performance.

By integrating realistic physical models, advanced control theory, and dedicated numerical tools, this work provides a robust framework for station-keeping analysis in low Earth orbit. The results offer insights into how drag and eclipse constraints shape optimal thrust strategies and contribute to the development of more efficient orbit maintenance techniques for future Earth observation and scientific missions.

1.4 Dissertation Overview

The remainder of this thesis is structured as follows:

- Chapter 2 Dynamical Models: introduces the mathematical models
 used to describe orbital motion. It begins with a review of classical orbital
 mechanics, reference frames, and orbital elements, and proceeds with the
 formulation of the equations of motion in spherical coordinates. Non-Keplerian
 perturbations, such as atmospheric drag and solar radiation pressure, are also
 discussed, together with the Sun-synchronous orbit geometry.
- Chapter 3 Optimal Control Theory: presents the theoretical background
 of optimal control and its application to orbital problems. The chapter
 discusses Pontryagin's Maximum Principle, the formulation of optimal control
 problems as boundary value problems, and the distinction between direct and
 indirect solution methods.
- Chapter 4 Problem Formulation and Implementation: details the specific problem addressed in this thesis, including the modeling of the discontinuous thrust constraint during eclipse, the structure of the boundary value problem, and the numerical solution approach. The implementation of the model within the extended *Oculus* framework and the development of the Python simulation tool with a graphical interface are also presented.
- Chapter 5 Results and Discussion: reports the results of the numerical simulations for three representative scenarios ideal dynamics, dynamics with atmospheric drag, and the full model including both drag and eclipse. The influence of these effects on optimal thrust profiles, orbital evolution, and mission performance is analyzed.
- Chapter 6 Conclusions and Future Work: summarizes the main findings of the thesis and outlines possible extensions, including the incorporation of additional perturbations, higher-fidelity gravity models, and more advanced control strategies.

Chapter 2

Dynamic Models

2.1 Introduction to Orbital Dynamics

The study of orbital dynamics is a cornerstone of modern astronautics, as it provides the mathematical and physical foundation for predicting and controlling the motion of spacecraft. Understanding these dynamics is essential not only for mission planning but also for the design of optimal trajectories, station-keeping strategies, and interplanetary transfers.

Orbital dynamics describe how a body moves under the influence of gravitational and non-gravitational forces. In the simplest approximation, the problem reduces to the motion of a particle around a central massive body, governed by Newton's law of gravitation. This framework, known as the two-body problem, offers analytical solutions for the motion of satellites and forms the basis for more complex models.

From Ideal Models to Perturbed Orbits

Although the two-body model provides valuable insights, real-world spacecraft trajectories are influenced by several perturbations:

- The Earth's non-spherical gravitational field (e.g., the J_2 term) causes secular variations of orbital elements such as the right ascension of the ascending node (RAAN) and argument of perigee.
- Atmospheric drag, which is particularly relevant for low Earth orbits (LEO), reduces the semi-major axis and increases the decay rate of the orbit.
- Solar radiation pressure and third-body effects (e.g., Moon and Sun) further modify the motion.

Accurate modeling of these effects is fundamental for missions requiring long-term orbit prediction or precision maneuvers, such as Sun-synchronous orbit maintenance or low-thrust trajectory optimization.

Relevance for This Work

The present thesis focuses on the station-keeping of a spacecraft in a Sun-synchronous orbit in LEO. This requires a detailed understanding of orbital dynamics in both ideal and perturbed conditions, with special emphasis on low-thrust control strategies. In the following sections, the two-body problem will be formulated, extended to spherical coordinates, and complemented by the description of relevant reference frames and perturbative forces.

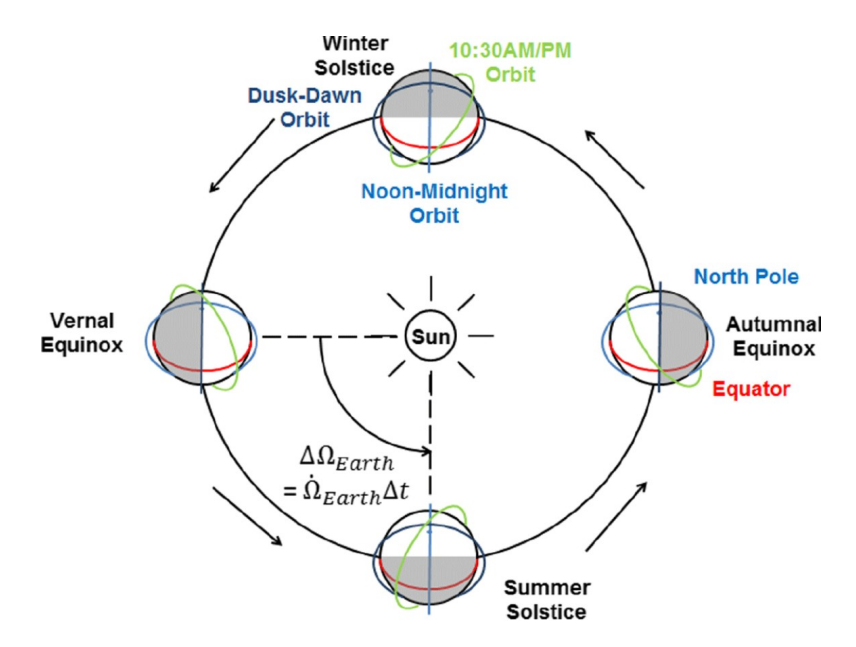


Figure 2.1: Example of SSO

2.2 Reference Frames and Transformations

A rigorous understanding of reference frames is fundamental in astrodynamics. Reference frames define how positions, velocities, and accelerations are described, and how transformations are performed for modeling, control, and ground-based operations. Here is the representation of some reference frames:

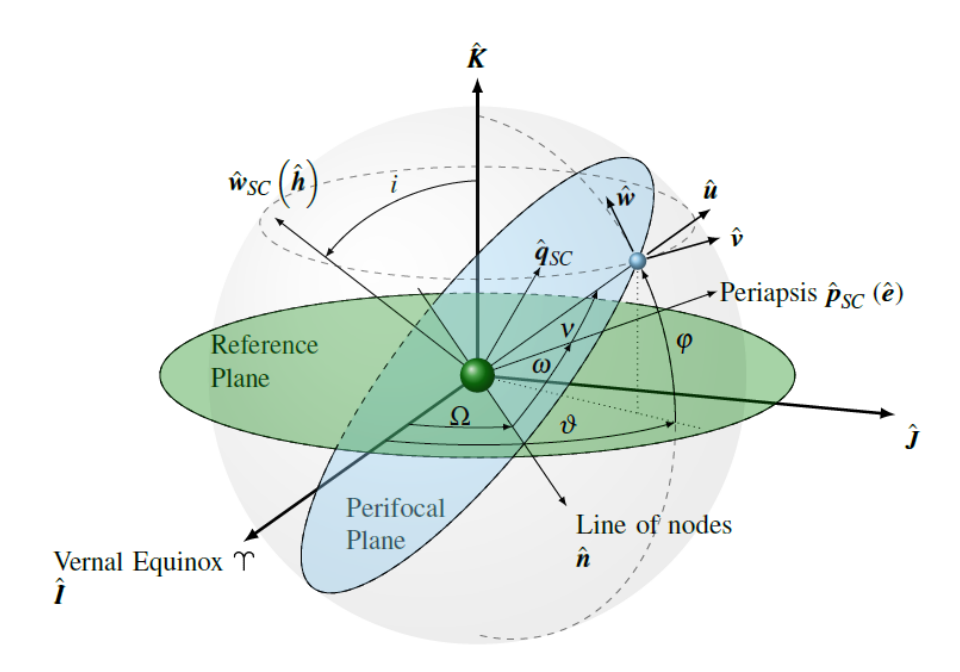


Figure 2.2: ECI, Perifocal, NEZ

Earth-Centered Inertial (ECI) Frame

The Earth-Centered Inertial (ECI) frame is a non-rotating inertial frame with its origin at the Earth's center of mass. It is typically aligned with the mean equator and equinox of the epoch J2000.

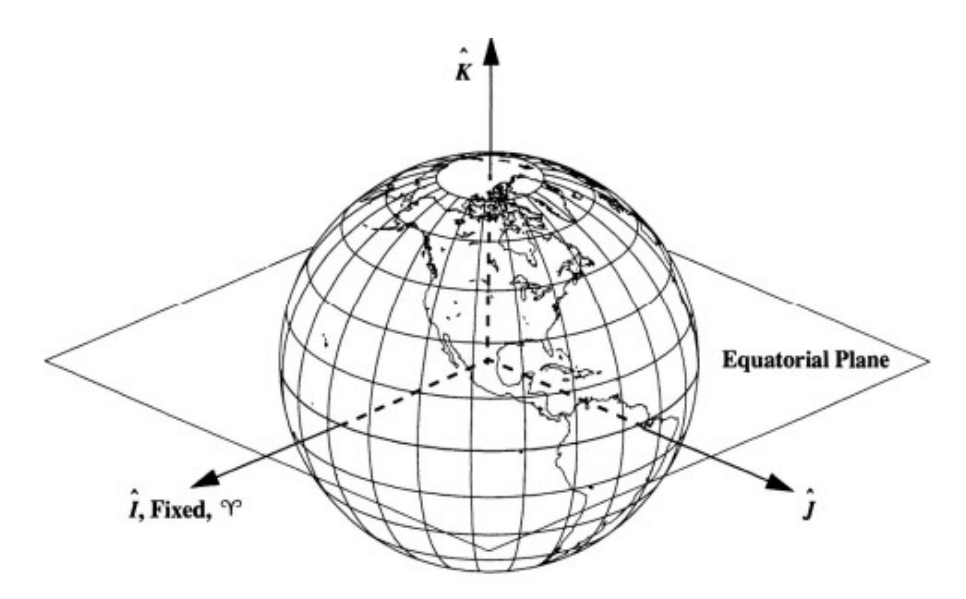


Figure 2.3: ECI

Its axes are:

• X-axis: Points towards the vernal equinox,

• **Z-axis**: Aligned with the Earth's rotational axis (North Pole),

• Y-axis: Completes the right-handed coordinate system.

The ECI frame is used as the inertial baseline for orbit propagation and optimal control formulations.

Earth-Centered Earth-Fixed (ECEF) Frame

The ECEF frame shares the same origin as the ECI, but it rotates with the Earth. It is fixed with respect to the Earth's surface, and thus convenient for expressing locations of ground stations or atmospheric models.

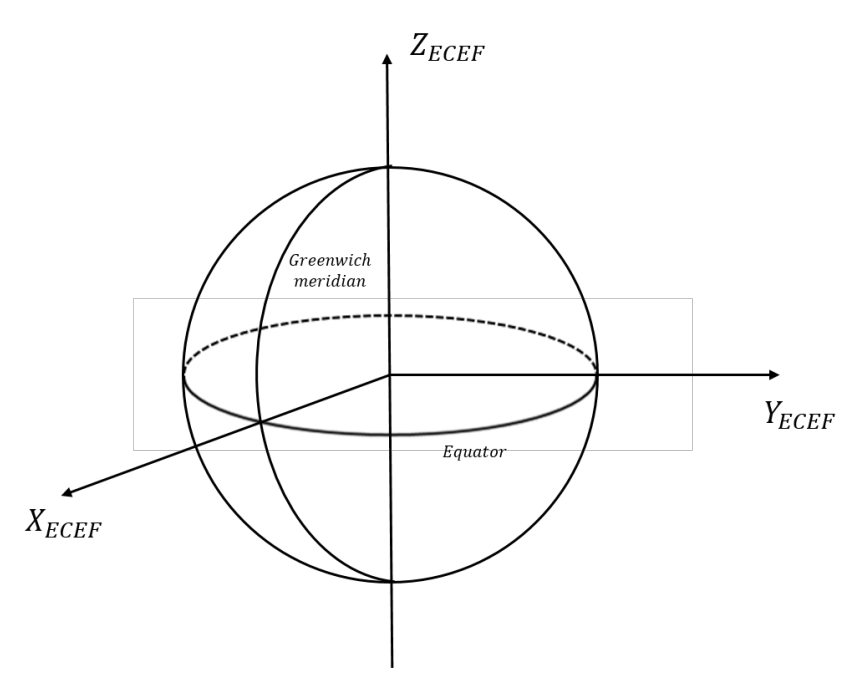


Figure 2.4: ECEF

The axes are:

- **X-axis**: Points towards the intersection of the equator and Greenwich meridian,
- **Z-axis**: Aligned with the North Pole,
- Y-axis: Completes the right-handed system.

NEZ (North-East-Zenith) Local Frame

The NEZ frame is a topocentric local reference frame centered at a specific point on the Earth's surface (e.g., a ground station).

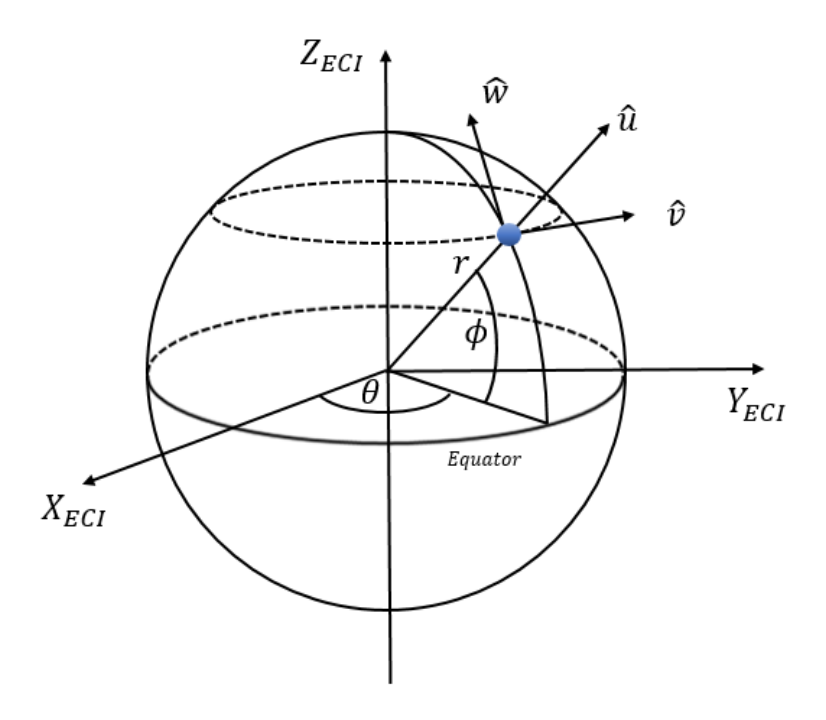


Figure 2.5: NEZ

The frame is defined by:

- N-axis: Points toward geographic north,
- E-axis: Points eastward along the local horizontal,
- **Z-axis**: Points upward, normal to the local tangent plane.

It is commonly used in ground tracking, navigation, and measurement systems.

Rotation Matrices and Reference Frame Transformations

The orientation of one reference frame with respect to another is defined by a combination of elementary rotations about the principal axes. A single rotation of

an angle θ about the x, y, or z axis is represented by the following matrices [1, 2]:

$$R_{1}(\theta) = \begin{bmatrix} 1 & 0 & 0 \\ 0 & \cos \theta & \sin \theta \\ 0 & -\sin \theta & \cos \theta \end{bmatrix}, R_{2}(\theta) = \begin{bmatrix} \cos \theta & 0 & -\sin \theta \\ 0 & 1 & 0 \\ \sin \theta & 0 & \cos \theta \end{bmatrix}, R_{3}(\theta) = \begin{bmatrix} \cos \theta & \sin \theta & 0 \\ -\sin \theta & \cos \theta & 0 \\ 0 & 0 & 1 \end{bmatrix}.$$
(2.1)

These matrices perform a passive rotation, i.e. they transform the components of a fixed vector from one reference frame to another rotated frame. The overall orientation between two right-handed orthogonal frames \mathcal{A} and \mathcal{B} can thus be expressed as:

$$\mathbf{r}_{\mathcal{B}} = R_{\mathcal{A} \to \mathcal{B}} \, \mathbf{r}_{\mathcal{A}}, \qquad R_{\mathcal{A} \to \mathcal{B}}^{-1} = R_{\mathcal{A} \to \mathcal{B}}^{\top}.$$

Below are the rotation conventions adopted in this work for the main frames used in orbital dynamics and ground applications.

ECI to ECEF The transformation between the Earth-Centered Inertial (ECI) frame and the Earth-Centered Earth-Fixed (ECEF) frame is obtained through a rotation about the z-axis of the Greenwich sidereal angle $\theta_G(t)$:

$$R_{ECI \to ECEF} = R_3(\theta_G(t)). \tag{2.2}$$

The angle θ_G represents the Earth's rotation about its polar axis and increases approximately linearly with time:

$$\theta_G(t) = \theta_{G0} + \omega_E t$$

where $\omega_E = 7.2921159 \times 10^{-5} \,\mathrm{rad/s}$ is the Earth's mean rotation rate. For high-precision applications, θ_G can be evaluated from the Julian Date using IAU/IERS conventions that include precession and nutation corrections [2].

This transformation is used to convert ground coordinates (latitude, longitude, altitude) or atmospheric fields—defined in the rotating ECEF frame—into the inertial frame employed for orbital propagation.

Perifocal (PQW) to ECI The perifocal reference frame $\{\hat{\mathbf{p}}, \hat{\mathbf{q}}, \hat{\mathbf{w}}\}$ is defined with origin at the central body and axes aligned with the orbital plane:

- $\hat{\mathbf{p}}$ points toward the periapsis;
- $\hat{\mathbf{q}}$ is orthogonal to $\hat{\mathbf{p}}$ in the orbital plane, completing a right-handed set;
- $\hat{\mathbf{w}}$ is normal to the orbital plane, parallel to the angular momentum vector.

The transformation from the perifocal frame to the inertial ECI frame is performed through the rotation sequence:

$$R_{POW \to ECI} = R_3(\Omega) R_1(i) R_3(\omega), \tag{2.3}$$

where Ω is the right ascension of the ascending node, i is the inclination, and ω is the argument of periapsis. This convention follows the standard 3–1–3 Euler rotation sequence [1, 2].

NEZ (North–East–Zenith) Local Frame For ground-based or topocentric analyses, it is convenient to define the local North–East–Zenith (NEZ) frame centered at a specific point on the Earth's surface. The transformation from ECEF to NEZ coordinates is constructed using the observer's geodetic latitude ϕ and longitude λ :

$$R_{ECEF \to NEZ} = \begin{bmatrix} -\sin\phi\cos\lambda & -\sin\phi\sin\lambda & \cos\phi \\ -\sin\lambda & \cos\lambda & 0 \\ -\cos\phi\cos\lambda & -\cos\phi\sin\lambda & -\sin\phi \end{bmatrix}. \tag{2.4}$$

The three axes are oriented as follows:

- \hat{N} : toward geographic north,
- \hat{E} : eastward along the local tangent plane,
- \hat{Z} : upward, normal to the local horizon.

The NEZ frame is mainly used to express measurements, elevation angles, and line-of-sight vectors between a satellite and a ground station.

Summary The rotation matrices introduced above enable consistent transformations among all the coordinate systems used in this work:

$$ECI \longleftrightarrow ECEF \longleftrightarrow NEZ, \quad PQW \longleftrightarrow ECI.$$

These transformations are fundamental for correctly describing satellite motion, evaluating eclipse conditions, and applying perturbations such as atmospheric drag or thrust in the appropriate reference frame.

Having defined the reference frames and rotation conventions, the next section derives the equations governing the two-body gravitational motion.

2.3 The Two-Body Problem

Model assumptions

Before deriving the governing equations of motion, it is important to state the assumptions underlying the classical two-body problem (2BP). The model represents the motion of two point masses, m_1 and m_2 , which interact only through their mutual gravitational attraction.

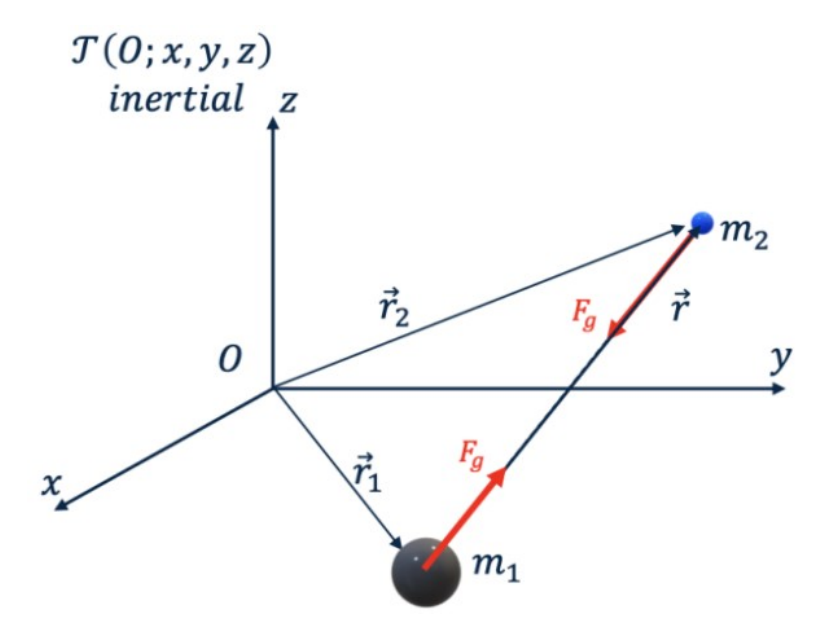


Figure 2.6: Two Body Problem scheme

The following hypotheses are introduced:

- Both bodies are considered **point masses**, meaning that their dimensions are negligible compared to the mutual distance, and the gravitational field is spherically symmetric.
- The system is **isolated**: no external forces act on the pair, such as atmospheric drag, solar radiation pressure, or third-body attractions.
- The gravitational constant G is uniform and time-invariant.
- The motion is analyzed in an **inertial reference frame** whose origin can be placed either at the system's barycenter or at one of the two bodies (typically the more massive one, in the Earth–satellite case).

Under these assumptions, the dynamics of the system are governed solely by Newton's law of universal gravitation and Newton's second law of motion [3, 2, 4].

Derivation of the relative equation of motion

Let m_1 denote the more massive body (e.g. the Earth) and m_2 the smaller one (e.g. a satellite). Their position vectors in an inertial reference frame are $\mathbf{R}_1(t)$ and $\mathbf{R}_2(t)$, respectively. The mutual gravitational forces acting on the two bodies are

$$\mathbf{F}_{12} = -G \frac{m_1 m_2}{\|\mathbf{R}_2 - \mathbf{R}_1\|^3} (\mathbf{R}_2 - \mathbf{R}_1), \qquad \mathbf{F}_{21} = -\mathbf{F}_{12},$$
 (2.5)

where \mathbf{F}_{12} is the force exerted by body 1 on body 2, and \mathbf{F}_{21} is the equal and opposite force on body 1. Applying Newton's second law to each mass yields

$$m_1 \ddot{\mathbf{R}}_1 = \mathbf{F}_{21}, \qquad m_2 \ddot{\mathbf{R}}_2 = \mathbf{F}_{12}.$$
 (2.6)

Subtracting the first equation from the second eliminates the internal forces and leads to the relative equation of motion. Defining the relative position vector $\mathbf{r} = \mathbf{R}_2 - \mathbf{R}_1$ and its second derivative $\ddot{\mathbf{r}} = \ddot{\mathbf{R}}_2 - \ddot{\mathbf{R}}_1$, one obtains

$$\ddot{\mathbf{r}} = -G\left(m_1 + m_2\right) \frac{\mathbf{r}}{r^3}, \qquad r = \|\mathbf{r}\|. \tag{2.7}$$

Equation (2.7) governs the relative motion of the two masses. It shows that each body moves under the influence of an inverse-square central force directed along \mathbf{r} . The term

$$\mu = G\left(m_1 + m_2\right)$$

is the gravitational parameter of the system. In the Earth–satellite case $m_2 \ll m_1$, so that $\mu \simeq G \, m_1 = 3.986 \, 004 \times 10^5 \, \mathrm{km}^3/\mathrm{s}^2$, known as the standard gravitational parameter of Earth. From this point on, the equations of motion will be expressed in terms of μ for compactness, leading to this formulation:

$$\ddot{\mathbf{r}} = -\frac{\mu}{r^3} \mathbf{r}.\tag{2.8}$$

Equation (2.8) forms the starting point for all orbital mechanics models. In the next sections it will be used to derive the integrals of motion (angular momentum and mechanical energy), and to obtain the analytical form of the orbital trajectory. These steps will ultimately lead to the classical conic solution $r = p/(1 + e \cos \nu)$, which describes all possible orbits under a central gravitational field [5, 6, 1].

Conservation Laws

A key property of the 2BP is that the force is always directed along \mathbf{r} , hence it is a *central force*. Taking the cross product of (2.7) with \mathbf{r} , the specific angular momentum vector

$$\mathbf{h} = \mathbf{r} \times \dot{\mathbf{r}} \tag{2.9}$$

is found to be constant, since $\dot{\mathbf{h}} = \mathbf{r} \times \ddot{\mathbf{r}} = \mathbf{0}$. This result implies that the motion is confined to the plane perpendicular to \mathbf{h} . Moreover, the rate at which the radius vector sweeps area, $\frac{1}{2} ||\mathbf{r} \times \dot{\mathbf{r}}|| = \frac{1}{2} h$, is constant. This is precisely *Kepler's second law*: equal areas are swept in equal times [3, 2].

Within this orbital plane we introduce polar coordinates (r, ν) , where ν is the *true* anomaly, the angle measured from the direction of the periapsis to the current position of the satellite. Expressing the velocity as $\dot{\mathbf{r}} = \dot{r} \, \hat{\mathbf{e}}_r + r \dot{\nu} \, \hat{\mathbf{e}}_{\nu}$, and substituting in (2.9) leads to $h = r^2 \dot{\nu}$, which directly relates angular velocity to instantaneous radius.

Differentiating \dot{r} and using (2.7), one obtains the radial and transverse components of acceleration:

$$\ddot{r} - r\dot{\nu}^2 = -\frac{\mu}{r^2}, \qquad r\ddot{\nu} + 2\dot{r}\dot{\nu} = 0.$$
 (2.10)

The second equation integrates immediately to the conservation law $r^2\dot{\nu}=h$ derived earlier. Substituting this expression in the radial equation of motion gives

$$\ddot{r} = \frac{h^2}{r^3} - \frac{\mu}{r^2}. (2.11)$$

It is convenient to introduce u=1/r and express derivatives with respect to the true anomaly ν . Since $\dot{r}=-h\frac{du}{d\nu}$ and $\ddot{r}=-h^2u^2\frac{d^2u}{d\nu^2}$, substituting into (2.11) yields the differential equation

$$\frac{d^2u}{d\nu^2} + u = \frac{\mu}{h^2},\tag{2.12}$$

whose general solution is

$$u(\nu) = \frac{\mu}{h^2} \Big[1 + e \cos(\nu - \nu_0) \Big]. \tag{2.13}$$

Choosing the reference such that $\nu_0 = 0$ at periapsis and recalling that u = 1/r, one obtains the classical polar equation of a conic section:

$$r = \frac{p}{1 + e \cos \nu}, \qquad p = \frac{h^2}{\mu}.$$
 (2.14)

Equation (2.14) demonstrates that all possible orbits under a central inverse-square law are conic sections with the Earth at one focus. The value of e (the eccentricity) determines the shape: e=0 corresponds to a circle, 0 < e < 1 to an ellipse, e=1 to a parabola, and e>1 to a hyperbola. For bound orbits (e<1), the relation between the specific mechanical energy and the semi-major axis is found by integrating the scalar product $\dot{\mathbf{r}} \cdot \dot{\mathbf{r}}$:

$$\mathcal{E} = \frac{v^2}{2} - \frac{\mu}{r} = -\frac{\mu}{2a},\tag{2.15}$$

known as the *vis-viva equation*. This compact expression directly relates the orbital velocity to position and semi-major axis, $v^2 = \mu(\frac{2}{r} - \frac{1}{a})$, and plays a central role in orbital transfers and energy analyses [4, 2].

To characterise the direction of periapsis within the orbital plane, it is useful to define the eccentricity vector

$$\mathbf{e} = \frac{\dot{\mathbf{r}} \times \mathbf{h}}{\mu} - \frac{\mathbf{r}}{r},\tag{2.16}$$

which is constant and points from the focus toward periapsis, with magnitude $\|\mathbf{e}\| = e$. The vector form of (2.14) can then be written as

$$\mathbf{r} = \frac{h^2/\mu}{1 + e\cos\nu}\,\hat{\mathbf{e}}_r,$$

revealing how the position vector rotates around the fixed **e** direction.

Finally, combining the angular momentum and energy integrals yields useful geometric relations:

$$h^2 = \mu a(1 - e^2), \qquad r_p = a(1 - e), \quad r_a = a(1 + e),$$

which fully specify the ellipse once (a, e) are known.

This formulation concludes the derivation of the unperturbed motion in closed form. Starting from Newton's laws, we have obtained the governing equation, identified the conserved quantities (\mathbf{h} and \mathcal{E}), and expressed the solution as a planar conic whose geometry depends solely on (a, e). These results represent the mathematical foundation upon which all subsequent perturbation and optimal-control analyses are constructed [1, 7, 5, 3].

2.4 Perturbation Models

2.4.1 Introduction to Perturbations

The two-body problem derived in Section 2.3 assumes a perfectly central gravitational field and neglects all secondary influences. In practice, the motion of an Earth-orbiting satellite is affected by several small forces, generally referred to as perturbations. These perturbations cause slow variations of the orbital elements over time, deviating the motion from the ideal Keplerian solution [3, 2, 5, 8].

Perturbations are traditionally classified as:

- Conservative, if they preserve the total mechanical energy of the orbit (e.g. the Earth's oblateness and third-body attractions);
- Non-conservative, if they dissipate energy from the system (e.g. atmospheric drag or magnetic torques).

The equation of motion can therefore be written as:

$$\ddot{\mathbf{r}} = -\frac{\mu}{r^3} \mathbf{r} + \mathbf{a}_p, \tag{2.17}$$

where \mathbf{a}_p collects all perturbing accelerations. For low Earth and Sun-synchronous orbits, the most relevant contributions are: the J_2 term of the geopotential, the atmospheric drag, and—at higher altitudes—the solar radiation pressure (SRP).

2.4.2 Zonal Harmonics and the J_2 Perturbation

Due to the Earth's equatorial bulge, the gravitational potential deviates from that of a perfect sphere and can be expanded as a series of zonal harmonics:

$$U(r,\phi) = -\frac{\mu}{r} \left[1 - \sum_{n=2}^{\infty} J_n \left(\frac{R_E}{r} \right)^n P_n(\sin \phi) \right], \qquad (2.18)$$

where R_E is the equatorial radius, ϕ the geocentric latitude, and P_n are the Legendre polynomials [2, 4].

Truncating the expansion at the dominant term $J_2 = 1.08263 \times 10^{-3}$ gives the quadrupole contribution:

$$U_{J_2} = -\frac{\mu}{r} J_2 \left(\frac{R_E}{r}\right)^2 \frac{1}{2} (3\sin^2 \phi - 1). \tag{2.19}$$

Taking the gradient of U_{J_2} produces the corresponding acceleration in the Earth-centered inertial (ECI) frame:

$$\mathbf{a}_{J_2} = \frac{3J_2\mu R_E^2}{2r^5} \begin{bmatrix} x(5z^2/r^2 - 1) \\ y(5z^2/r^2 - 1) \\ z(5z^2/r^2 - 3) \end{bmatrix}. \tag{2.20}$$

This acceleration acts in the orbital plane as a conservative perturbation, leading to secular precession of the line of nodes and the argument of perigee. Averaging the equations of motion over one orbital period yields the classical expressions:

$$\dot{\Omega} = -\frac{3}{2} J_2 n \left(\frac{R_E}{a}\right)^2 \frac{\cos i}{(1 - e^2)^2}, \qquad \dot{\omega} = \frac{3}{4} J_2 n \left(\frac{R_E}{a}\right)^2 \frac{(4 - 5\sin^2 i)}{(1 - e^2)^2}, \tag{2.21}$$

where $n = \sqrt{\mu/a^3}$ is the mean motion. These relations describe a westward regression of the ascending node and a rotation of the line of apsides, both depending on altitude and inclination [3, 9, 5, 8].

2.4.3 Application to Sun-Synchronous Orbits

Sun-synchronous orbits (SSO) exploit the nodal precession caused by J_2 to maintain a constant local solar time of passage over each point on Earth. By selecting a suitable combination of inclination and semi-major axis, the regression rate of the ascending node is synchronized with the apparent annual motion of the Sun:

$$\dot{\Omega}_{SSO} \approx -\frac{360^{\circ}}{\text{year}} = -1.991 \times 10^{-7} \,\text{rad/s}.$$
 (2.22)

Inserting (2.21) into the condition above yields:

$$\cos i_{SSO} = -\frac{2}{3J_2} \frac{(1 - e^2)^2}{(R_E/a)^2} \frac{\dot{\Omega}_{SSO}}{n}.$$
 (2.23)

For a representative altitude of $h=300~{\rm km}$ ($a\simeq 6671~{\rm km}$), this gives $i_{SSO}\approx 96.65^{\circ}$, corresponding to a retrograde, near-polar orbit [8, 5, 3]. Atmospheric drag slowly reduces the semi-major axis, thereby altering $\dot{\Omega}$ and breaking exact sun-synchronicity; small thrust maneuvers are therefore required for long-term maintenance.

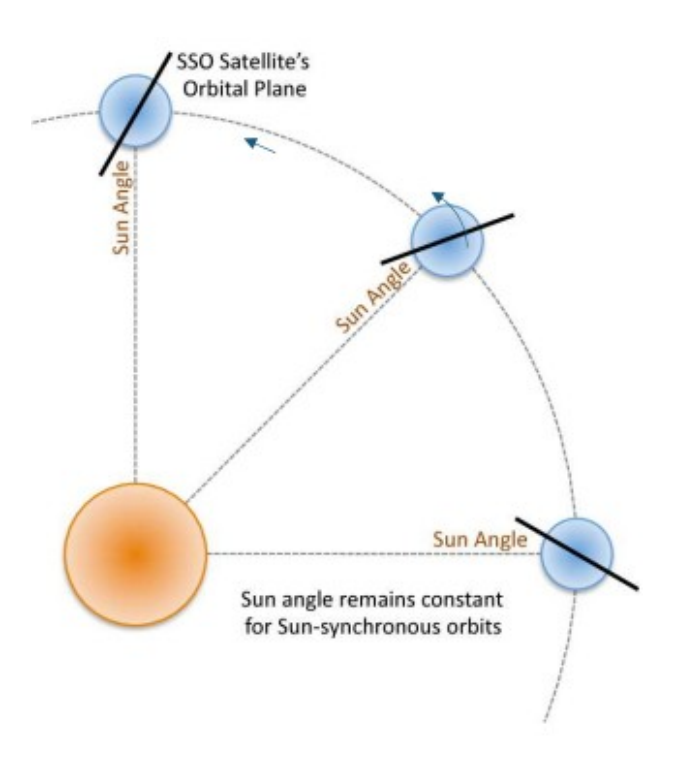


Figure 2.7: Condition for Sun-synchronicity: the J_2 -induced regression of the node matches the apparent motion of the Sun.

2.4.4 Atmospheric Drag

At low altitudes, typically below 800–1000 km, the residual atmosphere produces a drag acceleration opposed to the direction of motion, expressed as:

$$\mathbf{a}_D = -\frac{1}{2} \frac{C_D A}{m} \rho(h) v_{\text{rel}} \mathbf{v}_{\text{rel}}, \tag{2.24}$$

where C_D is the drag coefficient, A the reference area, m the satellite mass, and $\rho(h)$ the local atmospheric density. The velocity $\mathbf{v}_{\text{rel}} = \dot{\mathbf{r}} - \boldsymbol{\omega}_E \times \mathbf{r}$ accounts for the rotation of the atmosphere with the Earth.

In simplified textbooks an exponential model

$$\rho(h) = \rho_0 \, \exp\left(-\frac{h - h_0}{H}\right)$$

is often employed to approximate the density variation with altitude. While analytically convenient, this relation is *inadequate for accurate propagation* in low Earth orbits, as it neglects solar and geomagnetic activity and cannot reproduce the day—night asymmetry or temporal variations of the thermosphere. For this reason, in this work the density is computed using the PyMSIS implementation of the NRLMSISE-00 model [10], which provides $\rho(h,t)$ as a function of the solar flux indices (F10.7, F10.7a) and the geomagnetic index A_n .

The resulting drag acceleration is typically of the order of 10^{-6} – 10^{-7} m/s² in LEO, leading to a gradual decay of the semi-major axis and orbital energy. Unlike J_2 , this is a non-conservative perturbation and acts as a continuous dissipative force [5, 6, 1].

2.4.5 Solar Radiation Pressure

Beyond a few hundred kilometers of altitude, another perturbing effect becomes non-negligible: the *solar radiation pressure* (SRP). Photons emitted by the Sun carry momentum and exert a small but continuous force on exposed satellite surfaces. The resulting acceleration can be expressed as:

$$\mathbf{a}_{SRP} = -P_{\odot} C_R \frac{A}{m} \left(\frac{r_{\oplus}}{r_{\odot}}\right)^2 \hat{\mathbf{s}}, \tag{2.25}$$

where $P_{\odot}=4.56\times 10^{-6}\,\mathrm{N/m^2}$ is the solar radiation pressure at 1 AU, C_R is the reflectivity coefficient (typically 1–1.5), A/m the area-to-mass ratio, $\hat{\mathbf{s}}$ the unit vector from the Sun to the spacecraft, r_{\oplus} the mean Sun–Earth distance, and r_{\odot} the instantaneous Sun–spacecraft distance.

Although its magnitude is typically 10^{-7} – 10^{-8} m/s², SRP becomes significant for high area-to-mass spacecraft or during long-duration missions. In LEO the effect

is negligible compared to J_2 and drag, but it is often included in higher-fidelity propagation for completeness [2, 3].

In summary, the dynamical model implemented in this work explicitly includes the atmospheric drag as the only non-conservative perturbation acting on the satellite. The J_2 harmonic is not directly integrated as a force term but is employed analytically to determine the inclination ensuring the Sun-synchronous geometry of the reference orbit, according to Eq. (2.23).

Solar radiation pressure, although considerably weaker than drag in the altitude range of interest (300–500 km), may become comparable or even dominant for higher orbits or for spacecraft with large area-to-mass ratios. For this reason, it is here discussed for completeness but not included in the numerical propagation. Its long-term influence will, however, be relevant in higher-altitude missions and can be incorporated in future extensions of the model [2, 3].

Chapter 3

Optimal control theory

3.1 Introduction and Problem Definition

Optimal control theory provides a rigorous mathematical framework for determining how a dynamical system should be controlled in order to optimize a given performance objective. It extends classical control approaches by explicitly accounting for system dynamics, control constraints, and boundary conditions, allowing the identification of control strategies that achieve a desired goal in an optimal way.

In the context of dynamical systems, the goal of an optimal control problem (OCP) is to determine the time history of the control variables $\mathbf{u}(t)$ that minimizes (or maximizes) a given performance index while ensuring that the state vector $\mathbf{x}(t)$ evolves according to the prescribed dynamics. Formally, the system is described by a set of ordinary differential equations:

$$\dot{\mathbf{x}}(t) = \mathbf{f}(\mathbf{x}(t), \mathbf{u}(t), t), \tag{3.1}$$

where $\mathbf{x}(t) \in \mathbb{R}^n$ is the state vector, $\mathbf{u}(t) \in \mathbb{R}^m$ is the control vector, and \mathbf{f} is a generally nonlinear function describing the system dynamics.

The performance objective is expressed by a cost functional defined over a time interval $[t_0, t_f]$. In its most general form, known as the Bolza formulation, it is written as:

$$J = \Phi\left(\mathbf{x}(t_f), t_f\right) + \int_{t_0}^{t_f} L\left(\mathbf{x}(t), \mathbf{u}(t), t\right) dt,$$
(3.2)

where:

- $L(\mathbf{x}, \mathbf{u}, t)$ is the *running cost*, which accounts for contributions accumulated during the evolution of the system;
- $\Phi(\mathbf{x}(t_f), t_f)$ is the *terminal cost*, which depends on the final state and possibly on the final time.

The objective of the optimal control problem is to find the control law $\mathbf{u}^*(t)$ that minimizes J while satisfying the system dynamics, boundary conditions, and any constraints imposed on the state and control variables. The general formulation can therefore be expressed as:

$$\min_{\mathbf{u}(t)} J = \Phi\left(\mathbf{x}(t_f), t_f\right) + \int_{t_0}^{t_f} L\left(\mathbf{x}(t), \mathbf{u}(t), t\right) dt,$$
 (3.3)

subject to:
$$\dot{\mathbf{x}}(t) = \mathbf{f}(\mathbf{x}(t), \mathbf{u}(t), t),$$
 (3.4)

$$\mathbf{x}(t_0) = \mathbf{x}_0,\tag{3.5}$$

$$\mathbf{c}\big(\mathbf{x}(t), \mathbf{u}(t), t\big) \le \mathbf{0}. \tag{3.6}$$

The flexibility of this framework makes optimal control theory applicable to a wide variety of engineering problems, ranging from aerospace trajectory optimization and rendezvous maneuvers to mechanical systems, robotics, and economics. It provides a systematic way to handle dynamic constraints and performance tradeoffs, producing solutions that are not only feasible but provably optimal under the chosen cost criterion.

In the following sections, the mathematical foundations of optimal control theory are developed in detail. The general formulation introduced here will serve as the basis for deriving the necessary conditions for optimality through the Pontryagin Minimum Principle, determining the structure of the optimal control law, and establishing the boundary and path constraints that complete the formulation of the problem.

3.2 General Formulation of an Optimal Control Problem

The motion of a dynamical system controlled by external inputs can be described by a set of nonlinear differential equations of the form:

$$\dot{\mathbf{x}}(t) = \mathbf{f}(\mathbf{x}(t), \mathbf{u}(t), t), \qquad \mathbf{x}(t_0) = \mathbf{x}_0, \tag{3.7}$$

where:

- $\mathbf{x}(t) \in \mathbb{R}^n$ is the state vector describing the system at time t,
- $\mathbf{u}(t) \in \mathbb{R}^m$ is the control vector (decision variable),
- **f** is a continuous and sufficiently smooth function describing the system dynamics.

The goal of an optimal control problem (OCP) is to determine the control history $\mathbf{u}(t)$ that minimizes (or maximizes) a prescribed performance index while satisfying the state dynamics (3.7) and all boundary and path constraints.

Bolza, Mayer, and Lagrange Forms

The most general form of an optimal control problem is the *Bolza* form, written as:

$$J = \Phi(\mathbf{x}(t_f), t_f) + \int_{t_0}^{t_f} L(\mathbf{x}(t), \mathbf{u}(t), t) dt, \qquad (3.8)$$

where:

- $\Phi(\mathbf{x}(t_f), t_f)$ is the terminal cost (Mayer term), depending on the final state and possibly on the final time,
- $L(\mathbf{x}(t), \mathbf{u}(t), t)$ is the running cost (Lagrange term), defined over the control horizon $[t_0, t_f]$.

Two special cases of (3.8) are often considered:

• Mayer form: if L=0, the cost reduces to

$$J = \Phi(\mathbf{x}(t_f), t_f) \,,$$

i.e. only the terminal state contributes to the performance index.

• Lagrange form: if $\Phi = 0$, the cost is defined solely by the integral term:

$$J = \int_{t_0}^{t_f} L(\mathbf{x}(t), \mathbf{u}(t), t) dt.$$

It is always possible to convert a Bolza problem into either a Mayer or a Lagrange problem by introducing auxiliary states. For instance, by defining a new state variable

$$\dot{z}(t) = L(\mathbf{x}(t), \mathbf{u}(t), t), \quad z(t_0) = 0,$$

the Bolza problem (3.8) becomes equivalent to a Mayer problem:

$$J = \Phi(\mathbf{x}(t_f), t_f) + z(t_f).$$

Boundary Conditions

An optimal control problem is also defined by a set of boundary conditions on the state and possibly on the final time:

$$\mathbf{x}(t_0) = \mathbf{x}_0, \qquad \psi(\mathbf{x}(t_f), t_f) = \mathbf{0}.$$

The initial state is typically known and fixed, while the final conditions may be either fully prescribed (e.g. fixed orbital elements) or partially free (e.g. free final mass). In the latter case, transversality conditions will apply (see Section 3.3).

Path Constraints

In many practical applications, the state and control variables must satisfy additional *path constraints* during the evolution of the system:

$$\mathbf{g}(\mathbf{x}(t), \mathbf{u}(t), t) \leq \mathbf{0}.$$

These constraints may represent physical limits (e.g. thrust bounds), operational restrictions (e.g. thrust disabled in eclipse), or safety requirements (e.g. altitude limits). Path constraints significantly affect the structure of the optimal solution and must be properly handled in both analytical derivations and numerical implementations.

Time Horizon and Final Time

The final time t_f may be either fixed or free, depending on the mission objective. If it is treated as a free variable, its optimal value will emerge from the necessary conditions derived in the next section. Problems with free final time arise, for instance, in minimum-time transfers or when the mission duration is not prescribed a priori.

The general formulation described above provides the mathematical foundation for the derivation of necessary conditions for optimality, which can be obtained through the Pontryagin Minimum Principle (PMP) introduced in the next section [11, 12, 1].

3.3 Pontryagin Minimum Principle

The Pontryagin Minimum Principle (PMP) provides necessary conditions for optimality in continuous-time control problems and is a cornerstone of modern optimal control theory [13, 11, 12]. It extends the classical calculus of variations by introducing costate variables (also known as adjoint variables or Lagrange multipliers) associated with the system dynamics, transforming a constrained optimization problem into an unconstrained one.

Hamiltonian formulation

Consider the general optimal control problem introduced in Section 3.2:

$$\dot{\mathbf{x}}(t) = \mathbf{f}(\mathbf{x}(t), \mathbf{u}(t), t), \tag{3.9}$$

$$\mathbf{x}(t_0) = \mathbf{x}_0,\tag{3.10}$$

$$\mathbf{g}(\mathbf{x}(t), \mathbf{u}(t), t) \le \mathbf{0},\tag{3.11}$$

with cost functional in Bolza form:

$$J = \Phi(\mathbf{x}(t_f), t_f) + \int_{t_0}^{t_f} L(\mathbf{x}(t), \mathbf{u}(t), t) dt.$$
(3.12)

We define the *Hamiltonian function* as:

$$\mathcal{H}(\mathbf{x}, \mathbf{u}, \boldsymbol{\lambda}, t) = L(\mathbf{x}, \mathbf{u}, t) + \boldsymbol{\lambda}^{\mathsf{T}} \mathbf{f}(\mathbf{x}, \mathbf{u}, t), \tag{3.13}$$

where:

- $\lambda(t) \in \mathbb{R}^n$ is the costate vector introduced as a Lagrange multiplier associated with the dynamic constraint,
- **f** is the state dynamics vector defined in Eq. (3.7),
- L is the running cost defined in Eq. (3.8).

Necessary conditions for optimality

If $\mathbf{u}^*(t)$ is an optimal control and $\mathbf{x}^*(t)$ is the associated optimal trajectory, then there exists a nontrivial costate vector $\boldsymbol{\lambda}(t)$ such that the following necessary conditions hold for all $t \in [t_0, t_f]$:

State equations:

$$\dot{\mathbf{x}}^*(t) = \frac{\partial \mathcal{H}}{\partial \boldsymbol{\lambda}} \Big|_{(\mathbf{x}^*, \mathbf{u}^*, \boldsymbol{\lambda}^*)} = \mathbf{f}(\mathbf{x}^*, \mathbf{u}^*, t). \tag{3.14}$$

Costate equations:

$$\dot{\boldsymbol{\lambda}}^*(t) = -\frac{\partial \mathcal{H}}{\partial \mathbf{x}} \Big|_{(\mathbf{x}^*, \mathbf{u}^*, \boldsymbol{\lambda}^*)}.$$
 (3.15)

Stationarity condition:

$$\left. \frac{\partial \mathcal{H}}{\partial \mathbf{u}} \right|_{(\mathbf{x}^*, \mathbf{u}^*, \boldsymbol{\lambda}^*)} = \mathbf{0}. \tag{3.16}$$

For systems in which the control appears linearly in the Hamiltonian, condition (3.16) often leads to a bang-bang structure of the optimal control, which will be derived in Section 3.4.

Transversality conditions: The boundary conditions for the costate variables depend on the nature of the terminal constraints. If the final time is fixed and the terminal state is free, the costates satisfy:

$$\boldsymbol{\lambda}^{\top}(t_f) = \frac{\partial \Phi}{\partial \mathbf{x}(t_f)}.$$
 (3.17)

If some components of the final state are constrained, additional conditions involving Lagrange multipliers associated with these terminal constraints must be included. If the final time t_f is free, an additional transversality condition applies:

$$\mathcal{H}\left(\mathbf{x}^*(t_f), \mathbf{u}^*(t_f), \boldsymbol{\lambda}^*(t_f), t_f\right) + \frac{\partial \Phi}{\partial t_f} = 0.$$
(3.18)

3.3.1 Physical and mathematical interpretation of costates.

The costate variables $\lambda(t)$ arise naturally in the optimal control formulation as Lagrange multipliers associated with the system dynamics. Their introduction transforms the constrained optimization problem into an unconstrained one by embedding the dynamical equations directly into the Hamiltonian. Mathematically, they play a role analogous to that of generalized momenta in classical mechanics, being canonically conjugate to the state variables. In this sense, the pair (\mathbf{x}, λ) forms a Hamiltonian system whose evolution is governed by the PMP equations.

From a physical perspective, costates measure the sensitivity of the optimal performance index to changes in the state variables. Each component $\lambda_i(t)$ represents how a marginal variation in the state component $x_i(t)$ affects the total cost. For example, in orbital transfer problems, the components of the costate associated with velocity can be interpreted as generalized impulses or "shadow prices" of velocity, indicating the direction in which thrust should be applied to most effectively decrease the cost functional. Similarly, the costate associated with the mass variable reflects the sensitivity of the objective to changes in propellant mass, and its appearance in the switching function determines whether thrusting is beneficial or not.

Costates also carry important information about the structure of the optimal trajectory. In particular, discontinuities in the costate vector are associated with changes in active constraints or switching conditions in the control law. Moreover, their boundary values are directly linked to the terminal cost function through the transversality conditions, establishing a connection between the endpoint conditions and the evolution of the system throughout the trajectory. This dual role—mathematical and physical—makes costates a fundamental element of optimal control theory and central to the determination of the optimal solution [11, 12, 1].

Normal and abnormal solutions

Solutions to the PMP can be classified as:

- Normal solutions: when the multiplier associated with the cost functional is non-zero (often normalized to 1). These represent the typical case in most practical problems.
- **Abnormal solutions:** when the multiplier associated with the cost is zero. Although less common, they may arise in problems with pure constraints or singular arcs.

In this work, only normal solutions are considered, as they correspond to the physically meaningful fuel-optimal trajectories relevant to the orbital control problem addressed.

The PMP thus transforms the original optimal control problem into a two-point boundary value problem (TPBVP), consisting of the state equations (3.14), the costate equations (3.15), the stationarity condition (3.16), and the appropriate boundary and transversality conditions. The solution of this TPBVP yields both the optimal control law and the associated state trajectory. This theoretical framework serves as the foundation for the derivation of the control law in Section 3.4 [13, 11, 12, 1].

3.4 Optimal Control Law

This section derives the optimal thrust control law from the Pontryagin Minimum Principle (PMP), under the operational assumption that the thrust magnitude can only take two values: zero or the maximum available thrust T_{max} . The control is therefore characterized entirely by the unit thrust direction $\hat{\mathbf{u}}(t)$, which satisfies $\|\hat{\mathbf{u}}\| = 1$ when thrust is applied.

Hamiltonian structure

For the low-thrust orbital problem described by Eqs. (3.1)–(3.7) and a Mayer-type performance index (fuel-optimal formulation, i.e. maximize $m(t_f)$), the Hamiltonian can be written as:

$$\mathcal{H}(\mathbf{x}, \hat{\mathbf{u}}, T, \boldsymbol{\lambda}, t) = \boldsymbol{\lambda}_{\mathbf{r}}^{\top} \mathbf{v} + \boldsymbol{\lambda}_{\mathbf{v}}^{\top} \left(-\frac{\mu}{r^3} \mathbf{r} + \mathbf{a}_D + \frac{T}{m} \hat{\mathbf{u}} \right) + \lambda_m \left(-\frac{T}{I_{sp} g_0} \right), \quad (3.19)$$

where $\boldsymbol{\lambda} = [\boldsymbol{\lambda}_{\mathbf{r}}, \boldsymbol{\lambda}_{\mathbf{v}}, \lambda_m]^{\top}$ are the costates associated with the state variables $[\mathbf{r}, \mathbf{v}, m]^{\top}$.

Optimal thrust direction

For a given nonzero thrust magnitude, the Hamiltonian depends on the thrust direction $\hat{\mathbf{u}}$ only through the scalar product $\boldsymbol{\lambda}_{\mathbf{v}}^{\top}\hat{\mathbf{u}}$. The stationarity condition

$$\frac{\partial \mathcal{H}}{\partial \hat{\mathbf{u}}} = \mathbf{0}$$

subject to the unit norm constraint $\|\hat{\mathbf{u}}\| = 1$, leads to the well-known result:

$$\hat{\mathbf{u}}^*(t) = -\frac{\boldsymbol{\lambda}_{\mathbf{v}}(t)}{\|\boldsymbol{\lambda}_{\mathbf{v}}(t)\|}, \quad \text{when } T^*(t) > 0.$$
(3.20)

Hence, the optimal thrust direction is always antiparallel to the costate associated with the velocity, often referred to as the *primer vector*. This result has an intuitive physical meaning: thrust should always be applied in the direction that most efficiently reduces the Hamiltonian, which corresponds to pointing opposite to λ_{v} .

Bang-bang structure and switching function

By substituting Eq. (3.20) into Eq. (3.19), the thrust-dependent part of the Hamiltonian becomes:

$$\mathcal{H}_{\rm th}(T) = -T\left(\frac{\|\boldsymbol{\lambda}_{\mathbf{v}}\|}{m} + \frac{\lambda_m}{I_{sp}g_0}\right).$$

The necessary condition for optimality requires minimizing the Hamiltonian with respect to T. This leads naturally to the introduction of the *switching function*, defined as:

$$S_f(t) = \frac{\|\boldsymbol{\lambda}_{\mathbf{v}}(t)\|}{m(t)} + \lambda_m(t) \alpha, \qquad \alpha = \frac{1}{I_{sp}g_0}.$$
 (3.21)

The sign of $S_f(t)$ determines the optimal thrust policy:

$$T^*(t) = \begin{cases} T_{\text{max}}, & \text{if } S_f(t) > 0 \text{ and } \chi_{\text{sun}}(t) = 1, \\ 0, & \text{if } S_f(t) < 0 \text{ or } \chi_{\text{sun}}(t) = 0, \\ \text{either 0 or } T_{\text{max}}, & \text{if } S_f(t) = 0. \end{cases}$$
(3.22)

The physical interpretation of Eq. (3.21) is straightforward: the first term represents the dynamical benefit of applying thrust, linked to the velocity costate, while the second term accounts for the cost associated with propellant expenditure. When $S_f(t) > 0$, the dynamical benefit outweighs the mass penalty, and the optimal solution is to apply maximum thrust. Conversely, when $S_f(t) < 0$, the cost of thrusting exceeds its benefit and the optimal solution is to coast.

Additionally, the eclipse constraint, represented by the illumination function $\chi_{\text{sun}}(t)$, enforces the condition that no thrust can be applied while the spacecraft is in Earth's shadow, regardless of the value of $S_f(t)$.

It is worth noting that in optimal control problems where the control enters linearly into the Hamiltonian and the cost functional is purely Mayer, a continuous zero of $S_f(t)$ over a finite interval would correspond to a *singular arc*. In the fuel-optimal low-thrust problem considered here, with bounded thrust and discrete thrusting capability, singular arcs are not expected to occur. Coasting phases arise instead either from regions where $S_f(t) < 0$ or from eclipse intervals where thrusting is not permitted [11, 12].

Finally, combining Eqs. (3.20) and (3.22), the optimal control law is fully defined by the costate dynamics and the switching function:

$$\hat{\mathbf{u}}^*(t) = \begin{cases} -\frac{\boldsymbol{\lambda}_{\mathbf{v}}(t)}{\|\boldsymbol{\lambda}_{\mathbf{v}}(t)\|}, & \text{if } T^*(t) = T_{\text{max}}, \\ \text{arbitrary (unused)}, & \text{if } T^*(t) = 0, \end{cases}$$

with $T^*(t)$ given by Eq. (3.22). These results, together with the state and costate dynamics derived from the PMP, define the complete two-point boundary value problem equivalent to the original optimal control formulation. Its numerical solution will be addressed in Section 3.6 using indirect shooting and Newton-type methods [1, 11, 12].

3.5 Boundary Conditions and Constraints

The formulation of an optimal control problem is completed by specifying the boundary conditions and the constraints that the state and control variables must satisfy. These conditions, together with the necessary optimality conditions derived in the previous sections, define a well-posed two-point boundary value problem whose solution determines the optimal state trajectory and control profile.

Initial Conditions

The initial conditions describe the state of the system at the initial time t_0 . In most cases, the initial time is fixed and the initial state vector is fully specified:

$$\mathbf{x}(t_0) = \mathbf{x}_0. \tag{3.23}$$

The control input at the initial time is typically left free, unless additional physical or operational constraints require it to satisfy specific conditions. The choice of the initial state depends on the nature of the problem and on the physical system under consideration, but in all cases it serves as the starting point from which the system evolves according to the dynamics.

Final Conditions

The final conditions define the desired state of the system at the terminal time t_f . These conditions may be:

• Fixed terminal state: all components of the state vector are specified, i.e.

$$\mathbf{x}(t_f) = \mathbf{x}_f.$$

- Partially constrained terminal state: only some components are fixed, while others are free.
- Free terminal state: the final state is unconstrained and determined by the optimal solution.

The terminal time itself can also be treated in different ways:

- Fixed final time: t_f is prescribed.
- Free final time: t_f is a decision variable, and the transversality condition

$$\mathcal{H}\left(\mathbf{x}(t_f), \mathbf{u}(t_f), \boldsymbol{\lambda}(t_f), t_f\right) + \frac{\partial \Phi}{\partial t_f} = 0$$
(3.24)

must be satisfied.

The appropriate choice of terminal conditions depends on the specific control objective, such as reaching a target state, minimizing time, or optimizing fuel consumption.

Path Constraints

Path constraints represent limitations on the state and control variables that must hold throughout the trajectory. They are expressed as inequality or equality constraints of the form:

$$\mathbf{c}(\mathbf{x}(t), \mathbf{u}(t), t) \le \mathbf{0}, \quad t \in [t_0, t_f]. \tag{3.25}$$

Such constraints may arise from physical limitations, operational requirements, or safety considerations. Typical examples include:

• Control constraints: bounds on the control inputs, such as

$$\mathbf{u}_{\min} \leq \mathbf{u}(t) \leq \mathbf{u}_{\max}$$
.

• State constraints: restrictions on the state variables, for example to ensure that the system remains within a permissible region of the state space.

• Mixed constraints: involving both state and control variables simultaneously.

When active, path constraints modify the necessary conditions for optimality by introducing additional Lagrange multipliers associated with each active constraint. This leads to complementary slackness conditions that must be satisfied along the optimal trajectory.

Path constraints, together with the initial and terminal conditions, complete the mathematical formulation of the optimal control problem. Along with the system dynamics and cost functional, they define the feasible set in which the optimal trajectory must lie and allow the problem to be solved using the necessary conditions derived earlier [11, 12, 1].

3.6 Numerical Solution Approach

The application of the Pontryagin Minimum Principle transforms the original optimal control problem into a set of coupled differential equations for the state and costate variables, subject to boundary and transversality conditions. This results in a two-point boundary value problem (TPBVP) that must be solved to determine the optimal state trajectory and control profile. Analytical solutions are rarely available for nonlinear dynamical systems, making numerical methods the standard approach to solving such problems.

The Two-Point Boundary Value Problem

The TPBVP arising from the PMP consists of:

• the state differential equations:

$$\dot{\mathbf{x}}(t) = \frac{\partial \mathcal{H}}{\partial \boldsymbol{\lambda}},$$

• the costate differential equations:

$$\dot{\boldsymbol{\lambda}}(t) = -\frac{\partial \mathcal{H}}{\partial \mathbf{x}},$$

• the stationarity condition:

$$\frac{\partial \mathcal{H}}{\partial \mathbf{u}} = 0,$$

• the boundary and transversality conditions at t_0 and t_f .

This coupled system typically consists of 2n first-order differential equations, where n is the dimension of the state vector. The state equations are subject to initial conditions at t_0 , while the costate equations are subject to terminal conditions at t_f . This mixed set of boundary conditions is what characterizes the problem as a TPBVP.

Indirect Methods and the Shooting Approach

One of the most widely used approaches to solving TPBVPs arising from optimal control problems is the *indirect method*, where the necessary conditions derived from the PMP are integrated directly. The most common implementation of this approach is the *shooting method*.

The key idea is to convert the TPBVP into an equivalent *initial value problem* (IVP) by guessing the unknown initial values of the costates (and possibly other free parameters, such as the final time). The procedure can be outlined as follows:

- 1. Make an initial guess $\lambda(t_0)$ for the unknown costate vector at the initial time.
- 2. Integrate the combined state-costate system forward in time from t_0 to t_f using this guess.
- 3. Evaluate the terminal boundary conditions. If they are not satisfied, update the guess for $\lambda(t_0)$ and repeat.

This iterative process continues until the boundary conditions at t_f are met within a specified tolerance. The challenge lies in finding the correct initial costates, since small errors in the initial guess can lead to large deviations at the final time.

Newton Iteration and Sensitivity Matrix

To improve convergence, the shooting method is often implemented together with a Newton-type root-finding procedure. Let $\mathbf{F}(\lambda_0)$ be the vector of terminal constraint errors resulting from a given guess λ_0 . The goal is to solve:

$$\mathbf{F}(\boldsymbol{\lambda}_0) = \mathbf{0}.$$

A Newton iteration updates the costate guess according to:

$$\boldsymbol{\lambda}_0^{(k+1)} = \boldsymbol{\lambda}_0^{(k)} - \mathbf{J}^{-1} (\boldsymbol{\lambda}_0^{(k)}) \mathbf{F} (\boldsymbol{\lambda}_0^{(k)}), \qquad (3.26)$$

where **J** is the Jacobian matrix of partial derivatives of **F** with respect to λ_0 , also known as the *sensitivity matrix*. Its elements are given by:

$$J_{ij} = \frac{\partial F_i}{\partial \lambda_{0j}}.$$

Efficient and accurate computation of J is crucial for the convergence of the Newton iteration. It can be obtained by finite differences (perturbing the initial costates and re-integrating) or by integrating the variational equations associated with the TPBVP.

Multiple Shooting Method

In problems where the dynamics are highly nonlinear or the integration interval is long, the simple shooting method may suffer from numerical instability and poor convergence. An extension known as the *multiple shooting method* can alleviate these issues.

In multiple shooting, the integration interval $[t_0, t_f]$ is divided into N subintervals. Independent initial guesses are made for the state and costate vectors at the start of each subinterval, and the system is integrated separately within each segment. Additional continuity conditions are then imposed to ensure that the solutions match at the segment boundaries. This results in a larger but better-conditioned nonlinear system, which can improve convergence properties and numerical robustness.

Alternative Approaches

While indirect methods based on the PMP offer high accuracy and analytical insight, they require the solution of a potentially complex TPBVP and are sensitive to the initial costate guess. For this reason, direct methods are often employed as an alternative. These methods discretize the control and state trajectories and transcribe the continuous-time OCP into a finite-dimensional nonlinear programming (NLP) problem. Although they fall outside the scope of this chapter, direct approaches such as direct collocation and pseudospectral methods are widely used in practical trajectory optimization due to their robustness and ability to handle complex constraints [11, 12].

Overall, the numerical solution of optimal control problems formulated through the Pontryagin Minimum Principle ultimately reduces to solving a two-point boundary value problem. Among the available techniques, indirect methods such as shooting and multiple shooting remain fundamental tools due to their accuracy and close connection to the analytical structure of the problem.

Chapter 4

Dynamic Modeling and Optimal Control Formulation

4.1 Problem Setup and Modeling Framework

The theoretical framework presented in the previous chapter provides the necessary tools for formulating and solving optimal control problems in astrodynamics. In this chapter, the focus shifts from the general theory to its application to a specific class of problems: the optimal control of a satellite in Low Earth Orbit (LEO) using continuous low-thrust propulsion.

The goal is to construct a high-fidelity dynamical model that incorporates the relevant physical effects acting on a spacecraft in LEO and to integrate it into the optimal control formulation. In particular, the model is expressed in a three-dimensional spherical coordinate system and includes perturbations such as atmospheric drag and shadowing effects due to solar eclipses. These perturbations introduce additional challenges and constraints that must be accounted for in the control law.

Once the physical model has been defined, it is embedded within the optimal control problem and solved numerically using the indirect approach described previously. Finally, the chapter outlines the numerical implementation developed in Python and the structure of the graphical user interface (GUI) used to set up simulations and visualize results.

This transition from theory to application represents a crucial step toward the design of practical low-thrust station-keeping strategies and paves the way for the numerical results and analyses presented in the following chapters.

4.2 Dynamical Model Formulation

The spacecraft dynamics are formulated using a mixed representation that combines global position variables expressed in spherical coordinates with velocity and acceleration components expressed in a local reference frame. This approach preserves the advantages of a global inertial description while allowing a physically meaningful decomposition of forces and motion in a local basis.

Position Representation

The position of the spacecraft is expressed by the spherical coordinates (r, θ, ϕ) relative to the Earth-Centered Inertial (ECI) frame:

- r: geocentric distance from Earth's center;
- θ : measured eastward from the ECI X-axis and computed from the inertial components as

$$\theta = \arctan 2(y_{\text{ECI}}, x_{\text{ECI}});$$

• ϕ : geocentric latitude, measured from the equatorial plane and defined as

$$\phi = \arcsin\left(\frac{z_{\text{ECI}}}{r}\right).$$

Here, θ and ϕ are scalar quantities derived from the inertial position vector $\mathbf{r}_{\text{ECI}} = [x_{\text{ECI}}, y_{\text{ECI}}, z_{\text{ECI}}]^T$.

Local Reference Frame (NEZ)

For the description of velocity, thrust, and drag, a local orthonormal frame is defined at the spacecraft's instantaneous position. This frame is the North–East–Zenith (NEZ) system, constructed as:

- $\hat{\mathbf{e}}_Z$: zenith direction, aligned with the position vector \mathbf{r} and pointing radially outward from Earth;
- $\hat{\mathbf{e}}_E$: east direction, tangent to the parallel (line of constant latitude) and pointing eastward, orthogonal to both $\hat{\mathbf{e}}_Z$ and the Earth's rotation axis;
- $\hat{\mathbf{e}}_N$: north direction, tangent to the meridian and pointing toward increasing latitude.

This local basis is computed directly from the ECI position vector and Earth's rotation axis $\hat{\mathbf{k}}$ as:

$$\hat{\mathbf{e}}_Z = rac{\mathbf{r}}{\|\mathbf{r}\|}, \quad \hat{\mathbf{e}}_E = rac{\hat{\mathbf{k}} imes \hat{\mathbf{e}}_Z}{\|\hat{\mathbf{k}} imes \hat{\mathbf{e}}_Z\|}, \quad \hat{\mathbf{e}}_N = \hat{\mathbf{e}}_Z imes \hat{\mathbf{e}}_E$$

where $\hat{\mathbf{k}}$ is the unit vector along Earth's rotation axis.

Velocity Representation

The velocity vector \mathbf{v} is expressed as a linear combination of the NEZ unit vectors:

$$\mathbf{v} = u\,\hat{\mathbf{e}}_Z + v\,\hat{\mathbf{e}}_E + w\,\hat{\mathbf{e}}_N$$

where:

- u: radial velocity component along $\hat{\mathbf{e}}_Z$,
- v: eastward velocity component along $\hat{\mathbf{e}}_E$,
- w: northward velocity component along $\hat{\mathbf{e}}_N$.

It is worth emphasizing that $\hat{\mathbf{e}}_E$ points toward geographic east and is not, in general, aligned with the orbital velocity vector. This distinction is crucial when projecting perturbing accelerations and defining thrust directions.

Equations of Motion

The spacecraft motion under the effects of Earth's gravity, low-thrust propulsion, and atmospheric drag can be expressed as:

$$\dot{r} = u, \tag{4.1}$$

$$\dot{r} = u, \tag{4.1}$$

$$\dot{\theta} = \frac{v}{r\cos\phi}, \tag{4.2}$$

$$\dot{\phi} = \frac{w}{r},\tag{4.3}$$

$$\dot{u} = \frac{v^2 + w^2}{r} - \frac{\mu}{r^2} + a_{T,Z} + a_{D,Z},\tag{4.4}$$

$$\dot{v} = -\frac{uv}{r} - \frac{vw\tan\phi}{r} + a_{T,E} + a_{D,E},$$
 (4.5)

$$\dot{w} = -\frac{uw}{r} - \frac{v^2 \tan \phi}{r} + a_{T,N} + a_{D,N},\tag{4.6}$$

$$\dot{w} = -\frac{uw}{r} - \frac{v^2 \tan \phi}{r} + a_{T,N} + a_{D,N}, \tag{4.6}$$

$$\dot{m} = -\frac{T}{I_{sp}g_0}, \tag{4.7}$$

where: $-\mu = GM_E$ is Earth's gravitational parameter; $-a_{T,Z}$, $a_{T,E}$, $a_{T,N}$ are the thrust acceleration components along the zenith, east, and north directions; $-a_{D,Z}$, $a_{D,E}$, $a_{D,N}$ are the corresponding drag acceleration components; $-I_{sp}$ is the specific impulse and g_0 the standard gravitational acceleration.

The first three equations govern the evolution of the scalar coordinates (r, θ, ϕ) , while the next three describe the dynamics of the velocity components in the NEZ frame. The terms $\frac{v^2+w^2}{r}$ represent the centrifugal acceleration balancing gravity, while $-\frac{uv}{r}$ and $-\frac{uw}{r}$ arise from the curvature of the spherical coordinate system.

Physical Interpretation

This mixed representation — global coordinates for position and a local NEZ basis for velocity and acceleration — offers both physical clarity and computational convenience. The use of spherical coordinates ensures compatibility with ephemerides and eclipse geometry calculations in the inertial frame, while the NEZ decomposition provides a natural description of thrust and perturbing forces. Atmospheric drag acts primarily in the $\hat{\mathbf{e}}_Z$ direction, while thrust can be oriented with respect to $\hat{\mathbf{e}}_Z$, $\hat{\mathbf{e}}_E$, and $\hat{\mathbf{e}}_N$ to achieve the desired orbital control.

4.3 Atmospheric Drag Modeling

Atmospheric drag is one of the most significant perturbations affecting satellites in Low Earth Orbit (LEO). Unlike high-altitude missions, where the atmosphere is practically negligible, satellites operating below approximately 1000 km experience a continuous decelerating force due to interactions with the rarefied atmosphere. Over time, this drag leads to a reduction in orbital energy and altitude, making it a critical effect to account for in trajectory design and station-keeping strategies.

Fundamentals of Drag Acceleration

The aerodynamic drag force experienced by a satellite traveling through the upper atmosphere is given by:

$$\mathbf{F}_D = -\frac{1}{2} C_D A \rho v_{\text{rel}} \mathbf{v}_{\text{rel}}, \tag{4.8}$$

where:

- C_D is the drag coefficient, dependent on the spacecraft geometry and flow regime;
- A is the effective cross-sectional area of the spacecraft;
- ρ is the atmospheric density at the current altitude;

- $\mathbf{v}_{\rm rel}$ is the relative velocity between the spacecraft and the surrounding atmosphere;
- $v_{\text{rel}} = \|\mathbf{v}_{\text{rel}}\|$ is its magnitude.

The corresponding acceleration is obtained by dividing by the spacecraft mass:

$$\mathbf{a}_D = -\frac{1}{2} C_D \frac{A}{m} \rho v_{\text{rel}} \mathbf{v}_{\text{rel}}.$$
 (4.9)

The relative velocity accounts for the fact that the atmosphere rotates with the Earth. If ω_{\oplus} is Earth's rotation vector, then:

$$\mathbf{v}_{\mathrm{rel}} = \mathbf{v} - \boldsymbol{\omega}_{\oplus} \times \mathbf{r}.$$

Atmospheric Density Modeling

A key challenge in modeling drag is the determination of atmospheric density ρ , which varies with altitude, solar activity, geomagnetic conditions, latitude, local time, and season. Inaccurate density modeling can lead to significant errors in drag prediction and orbit propagation.

A commonly used simplified model expresses the density as an exponential function of altitude:

$$\rho(h) = \rho_0 \exp\left(-\frac{h - h_0}{H}\right),\tag{4.10}$$

where ρ_0 is the reference density at altitude h_0 , and H is the scale height. This model is attractive due to its simplicity and analytical form, but it neglects many physical influences such as solar flux variability, diurnal variations, and compositional changes in the upper atmosphere. As a result, its accuracy rapidly deteriorates above about 300 km, often producing errors of one order of magnitude or more.

To achieve higher fidelity, this work employs the NRLMSISE-00 empirical atmospheric model, implemented via the pymsis library [10]. This model accounts for variations due to solar flux $(F_{10.7})$, geomagnetic index (A_p) , and local time, and has been widely validated for orbital prediction applications. The density is computed as a function of position and time:

$$\rho = \rho(r, \theta, \phi, t; F_{10.7}, A_p), \tag{4.11}$$

where the arguments explicitly indicate the dependence on position, epoch, and space weather parameters.

Direct calls to MSISE-00 at each integration step, however, can be computationally expensive. To address this, we adopt a hybrid approach in which the density is precomputed over a grid of altitudes and stored in a table. During integration, ρ

is obtained by interpolation from this tabulated data. This method preserves the fidelity of the original model while substantially reducing runtime.

The advantages of this approach are illustrated in Figure 4.1. The plot compares the density as a function of altitude predicted by the exponential model, the interpolated tabulated MSISE-00, and the "true" MSISE-00 output. The exponential model diverges significantly from the true profile beyond 300 km, while the interpolated version overlaps almost perfectly with the reference curve.

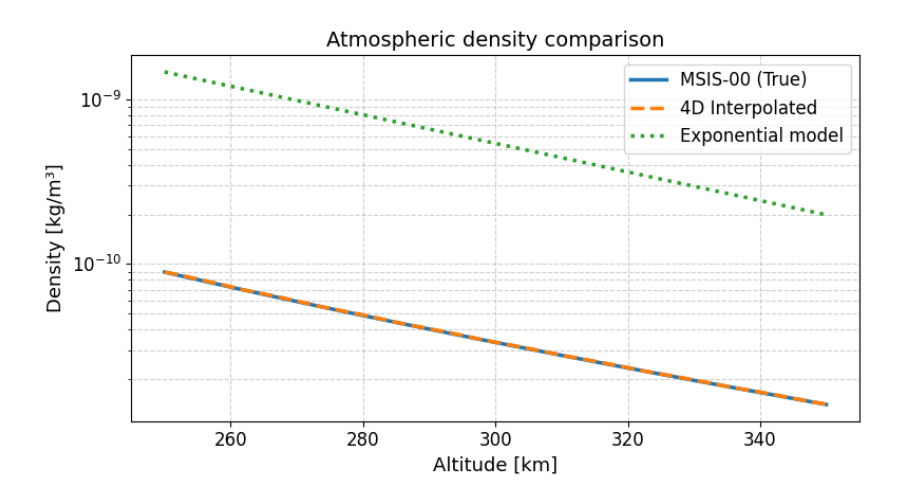


Figure 4.1: Comparison between the exponential model, tabulated-interpolated MSISE-00, and the reference MSISE-00 output.

A second way to quantify model accuracy is to examine the relative error in density prediction:

$$\varepsilon_{\rho}(h) = \frac{|\rho_{\text{model}}(h) - \rho_{\text{MSIS}}(h)|}{\rho_{\text{MSIS}}(h)}.$$

As shown in Figure 4.2, the exponential model exhibits large errors, whereas the interpolated version maintains errors well below a few percent over the entire range of interest.

Because the drag acceleration

$$\mathbf{a}_D = -\frac{1}{2} C_D \frac{A}{m} \rho \, v_{\text{rel}} \, \mathbf{v}_{\text{rel}}$$

depends linearly on ρ , these density errors translate directly into proportional errors in the computed drag force.

For these reasons, the tabulated-interpolated NRLMSISE-00 model was adopted in this work as the best compromise between accuracy and computational efficiency. Its use ensures that drag effects are represented realistically while preserving acceptable integration times during optimal control simulations.

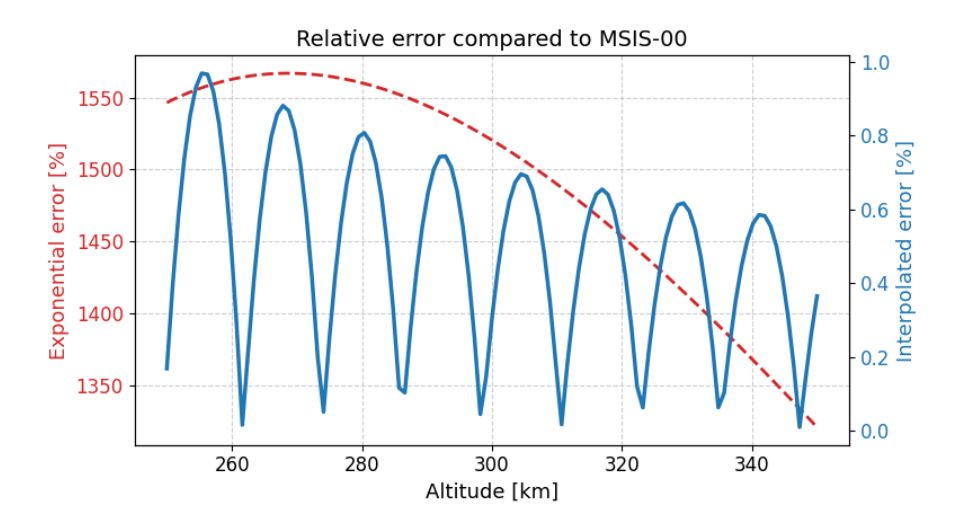


Figure 4.2: Relative error density.

Acceleration Components in Spherical Coordinates

In the spherical coordinate system adopted in this work, the drag acceleration is projected onto the ZEN directions. Denoting by $\hat{\mathbf{Z}}, \hat{\mathbf{E}}, \hat{\phi}$ the local unit vectors, the acceleration can be written as:

$$\mathbf{a}_D = a_{D,Z} \hat{\mathbf{Z}} + a_{D,E} \hat{\mathbf{E}} + a_{D,N} \hat{\mathbf{N}}, \tag{4.12}$$

where the components are obtained by projecting \mathbf{a}_D onto each basis vector. These components are then included in the dynamical equations introduced in Section 4.2, where they act as perturbing terms in the radial, in-plane, and out-of-plane equations of motion.

Accurate modeling of drag is essential in low-thrust orbit control problems, as it directly affects the energy balance and long-term orbital evolution. In particular, it influences the required thrust magnitude and direction needed to counteract orbital decay and maintain mission requirements over extended durations.

4.4 Eclipse Modeling and Sun Visibility

Accurate detection of eclipse intervals is essential in low-thrust mission analysis because solar power availability directly affects the admissible thrusting arcs. This section formulates the Sun visibility test in an Earth-centered inertial (ECI) frame using a conical shadow model (umbra/penumbra) and, for comparison, a simpler cylindrical approximation [2, 14].

Geometry and definitions

Let $\mathbf{r}(t) \in \mathbb{R}^3$ be the spacecraft position vector expressed in ECI and $\mathbf{r}_{\odot}(t)$ the geocentric Sun position (from ephemerides). Define the Sun unit vector and its geocentric distance as

$$\hat{\mathbf{e}}_{\odot}(t) = \frac{\mathbf{r}_{\odot}(t)}{\|\mathbf{r}_{\odot}(t)\|}, \qquad k(t) = \|\mathbf{r}_{\odot}(t)\|.$$

Let R_{\oplus} and R_{\odot} denote the mean radii of Earth and Sun, respectively. Introduce the axial coordinate along the anti-solar direction and the distance from the Sun–Earth axis:

$$d(t) = -\mathbf{r}(t) \cdot \hat{\mathbf{e}}_{\odot}(t), \qquad \rho(t) = \|\mathbf{r}(t) - (\mathbf{r}(t) \cdot \hat{\mathbf{e}}_{\odot}(t))\|. \tag{4.13}$$

Thus d > 0 identifies the anti-solar (night) side; ρ is the perpendicular distance to the axis.

Conical shadow model (umbra/penumbra)

Finite solar angular size produces a conical umbra and a surrounding penumbra. Their axial lengths are

$$L_u(t) = \frac{k(t) R_{\oplus}}{R_{\odot} - R_{\oplus}}, \qquad L_p(t) = \frac{k(t) R_{\oplus}}{R_{\odot} + R_{\oplus}}, \tag{4.14}$$

and the corresponding cone radii at distance $d \ge 0$ from Earth's center (measured along $-\hat{\mathbf{e}}_{\odot}$) are

$$R_u(d) = R_{\oplus} \left(1 - \frac{d}{L_u} \right) \quad (0 \le d \le L_u), \qquad R_p(d) = R_{\oplus} \left(1 + \frac{d}{L_p} \right) \quad (d \ge 0).$$
(4.15)

The illumination status follows directly:

$$\chi_{\text{sun}}(t) = \begin{cases} 0, & d(t) \ge 0 \text{ and } \rho(t) \le R_u(d(t)) \text{ (umbra)}, \\ \chi_{\text{pen}}, & d(t) \ge 0 \text{ and } R_u(d(t)) < \rho(t) \le R_p(d(t)) \text{ (penumbra)}, \\ 1, & \text{otherwise.} \end{cases}$$

$$(4.16)$$

Here $\chi_{\text{pen}} \in (0,1)$ may be set to 0 (conservative assumption: no thrust in penumbra) or to a user-defined fraction if a partial-power model is desired. In many preliminary analyses, both umbra and penumbra are treated as eclipse ($\chi_{\text{sun}} = 0$).

Cylindrical approximation (parallel rays)

For fast computations, the cylindrical shadow model neglects solar angular size (parallel rays). The spacecraft is in shadow iff it lies on the night side and within a cylinder of radius R_{\oplus} aligned with $-\hat{\mathbf{e}}_{\odot}$:

$$\chi_{\text{sun}}^{\text{cyl}}(t) = \begin{cases} 0, & \mathbf{r} \cdot \hat{\mathbf{e}}_{\odot} < 0 \text{ and } \rho(t) \le R_{\oplus}, \\ 1, & \text{otherwise.} \end{cases}$$
 (4.17)

This approximation overestimates eclipse duration slightly relative to the conical model, but is often acceptable for preliminary screening.

Sun vector and frames

High-precision Sun position $\mathbf{r}_{\odot}(t)$ is obtained from ephemerides (e.g. NAIF SPICE) and transformed to the ECI frame used in the dynamics. Care must be taken to use a consistent time scale and reference frame (e.g. converting from the ephemeris frame to ECI/J2000) to avoid phase errors in eclipse entry/exit times [14, 2].

Event detection in numerical integration

Eclipse transitions are identified by locating the roots of the implicit surfaces $\rho = R_u(d)$ (umbra boundary) and $\rho = R_p(d)$ (penumbra boundary) with $d \ge 0$. In practice, one monitors the signed functions

$$\Phi_u(t) = \rho(t) - R_u(d(t)), \qquad \Phi_p(t) = \rho(t) - R_p(d(t)),$$

and triggers events when their sign changes, updating $\chi_{\text{sun}}(t)$ according to Eq. (4.16). This yields consistent, time-accurate eclipse arcs within the integration scheme.

4.5 Optimal Control Problem Formulation for the LEO Scenario

With the physical model and perturbations established in the previous sections, the optimal control problem can now be formulated for a satellite operating in Low Earth Orbit (LEO) under continuous low-thrust propulsion. The objective is to determine the thrust direction that minimizes propellant consumption (or equivalently maximizes final mass) while maintaining the desired orbital configuration in the presence of drag and eclipse constraints.

State and Control Variables

The state vector is defined as:

$$\mathbf{x}(t) = \begin{bmatrix} r(t) \\ \theta(t) \\ \phi(t) \\ u(t) \\ v(t) \\ w(t) \\ w(t) \\ m(t) \end{bmatrix}, \tag{4.18}$$

where r, θ, ϕ are the spherical position coordinates, u, v, w are the velocity components, and m is the spacecraft mass.

The control vector consists of the thrust direction, expressed through two control angles:

$$\mathbf{u}(t) = \begin{bmatrix} \alpha(t) \\ \delta(t) \end{bmatrix},\tag{4.19}$$

where α is the in-plane angle and δ the out-of-plane angle of the thrust vector. The thrust magnitude is assumed constant and equal to T_{max} when the engine is active and zero otherwise.

System Dynamics with Perturbations

The state dynamics including gravitational acceleration, atmospheric drag, and low-thrust propulsion are the same described in the section 4.2. For the calculation of the variation of the mass we had to ad the $\chi_{\text{sun}}(t)$, where $\chi_{\text{sun}}(t)$ is the illumination function defined in Eq. (4.16), equal to 1 in sunlight and 0 during eclipse. This function acts as a control constraint, enforcing the physical condition that the thruster cannot operate without solar power.

Objective Functional

The cost functional is chosen to maximize the final mass, or equivalently, to minimize propellant consumption:

$$J = -m(t_f). (4.20)$$

This formulation belongs to the Mayer class of optimal control problems, where the cost depends only on the final state. Alternative formulations could include Lagrange terms (e.g., minimizing time or integrated thrust), but the Mayer form is particularly suited for low-thrust station-keeping missions where fuel efficiency is critical.

Hamiltonian and Optimality Conditions

The Hamiltonian associated with this problem is:

$$\mathcal{H} = \lambda_r u + \lambda_\theta \frac{v}{r \cos \phi} + \lambda_\phi \frac{w}{r}$$

$$+ \lambda_u \left(\frac{v^2 + w^2}{r} - \frac{\mu}{r^2} + a_{T,Z} + a_{D,Z} \right)$$

$$+ \lambda_v \left(-\frac{uv}{r} - \frac{vw \tan \phi}{r} + a_{T,E} + a_{D,E} \right)$$

$$+ \lambda_w \left(-\frac{uw}{r} + \frac{v^2 \tan \phi}{r} + a_{T,N} + a_{D,N} \right) - \lambda_m \frac{T_{\text{max}}}{I_{sp}g_0} \chi_{\text{sun}}(t)$$

$$(4.21)$$

where $\boldsymbol{\lambda} = [\lambda_r, \lambda_\theta, \lambda_\phi, \lambda_u, \lambda_v, \lambda_w, \lambda_m]^T$ is the costate vector associated with the state variables.

The necessary condition for optimality is obtained by setting the partial derivative of the Hamiltonian with respect to the control direction to zero:

$$\frac{\partial \mathcal{H}}{\partial \alpha} = 0, \qquad \frac{\partial \mathcal{H}}{\partial \delta} = 0.$$

Introducing the switching function:

$$S_f(t) = \sqrt{(\lambda_u \cos \alpha \cos \delta + \lambda_v \sin \alpha \cos \delta + \lambda_w \sin \delta)^2} - \frac{\lambda_m}{I_{sn}g_0}, \quad (4.22)$$

the optimal thrusting condition is:

$$T(t) = \begin{cases} Tmax, & S_f(t) > 0, \\ 0, & S_f(t) < 0. \end{cases}$$
 (4.23)

This condition enforces thrusting only when the marginal benefit of propellant expenditure exceeds its cost, and it is further modulated by the illumination function, which prevents thrust during eclipse phases regardless of the switching function sign.

Boundary Conditions and Constraints

The initial state is prescribed by the mission scenario:

$$\mathbf{x}(t_0) = \mathbf{x}_0, \tag{4.24}$$

while the terminal state may be either fully or partially constrained depending on the mission requirements. Typical constraints include maintaining the orbital radius or ground-track repeatability within specified tolerances.

Path constraints are also imposed:

- Thrust is limited: T = 0 or Tmax;
- Thrust is disabled during eclipse: T=0 if $\chi_{\text{sun}}(t)=0$;
- State constraints (e.g., altitude limits) may be included depending on the operational scenario.

Together, these elements define a well-posed optimal control problem tailored to a realistic LEO environment with continuous low thrust, atmospheric drag, and eclipse constraints.

4.6 Numerical Implementation

The optimal control problem formulated in Section 4.5 cannot be solved analytically due to the nonlinear dynamics, the presence of perturbations such as atmospheric drag, and the time-dependent eclipse constraint. Instead, it must be solved numerically by integrating the necessary conditions derived from the Pontryagin Minimum Principle. This leads to a two-point boundary value problem (TPBVP) that is solved using an indirect approach based on the shooting method combined with Newton iteration.

Problem Transformation and State Augmentation

The first step is to rewrite the optimal control problem as an augmented dynamical system composed of both state and costate equations:

$$\frac{d}{dt} \begin{bmatrix} \mathbf{x}(t) \\ \boldsymbol{\lambda}(t) \end{bmatrix} = \begin{bmatrix} \frac{\partial \mathcal{H}}{\partial \boldsymbol{\lambda}} \\ -\frac{\partial \mathcal{H}}{\partial \mathbf{x}} \end{bmatrix},$$

where the control enters implicitly through the switching function and is determined at each time step by enforcing the stationarity condition.

This system, consisting of 2n first-order differential equations (with n=7 in our case), is integrated forward in time starting from known initial conditions for the state and a guessed initial condition for the costates.

Shooting Method and Costate Guessing

Because the state vector is constrained at the initial time and the costate vector is constrained at the final time, the problem is inherently a TPBVP. The shooting method converts it into an initial value problem by guessing the unknown initial costates $\lambda(t_0)$. The algorithm proceeds as follows:

- 1. Make an initial guess $\lambda^{(0)}(t_0)$ for the costate vector.
- 2. Integrate the augmented system forward in time from t_0 to t_f using a numerical ODE solver.
- 3. Evaluate the terminal boundary conditions (e.g., final radius, velocity, or ground-track phase).
- 4. If the boundary conditions are not satisfied, update $\lambda(t_0)$ using a Newton-type iteration and repeat until convergence.

The accuracy of the initial guess strongly influences convergence. A poor initial guess may result in divergence or convergence to a non-optimal solution. In practical applications, the initial guess can be generated by simplified analytical approximations, by linearizing the dynamics, or by using solutions from neighboring problems as warm starts.

Newton Iteration and Sensitivity Matrix

The update of the costate guess is performed via a Newton iteration. Denoting by $\mathbf{F}(\lambda_0)$ the vector of boundary condition errors resulting from a given initial guess, the root-finding problem is:

$$\mathbf{F}(\boldsymbol{\lambda}_0) = \mathbf{0}.$$

The costate vector is updated iteratively as:

$$\boldsymbol{\lambda}_0^{(k+1)} = \boldsymbol{\lambda}_0^{(k)} - \mathbf{J}^{-1} \left(\boldsymbol{\lambda}_0^{(k)} \right) \mathbf{F} \left(\boldsymbol{\lambda}_0^{(k)} \right), \tag{4.25}$$

where \mathbf{J} is the Jacobian (sensitivity) matrix:

$$\mathbf{J}_{ij} = \frac{\partial F_i}{\partial \lambda_{0j}}.$$

The Jacobian can be computed numerically by finite differences, i.e., perturbing each costate component and reintegrating the system, or analytically by integrating the variational equations. The latter improves accuracy but requires additional implementation effort.

Time Integration Scheme

The forward integration of the state–costate system is carried out using a variable-step Runge–Kutta integrator of order 4(5), such as Dormand–Prince (RK45). Variable step-size control is crucial because the problem exhibits regions of different time scales — for example, near eclipse transitions or during thrust switches — where fine resolution is necessary to ensure numerical stability and accuracy.

At each time step, the switching function is evaluated and used to determine whether thrust is applied. The illumination function $\chi_{\text{sun}}(t)$ is also evaluated in real time based on the Sun–Earth–spacecraft geometry (Section 4.4) to enforce the eclipse constraint. This results in a time-varying control law that respects physical constraints.

Handling Path Constraints

Path constraints such as thrust availability in sunlight and thrust magnitude limits are enforced directly during integration. The thrust magnitude is set to T_{max} if the switching function is positive and $\chi_{\text{sun}}(t) = 1$, and to zero otherwise. This logic ensures that the control solution remains physically admissible and consistent with the spacecraft's power limitations.

Inequality constraints on state variables (e.g., altitude or latitude limits) can be treated either by penalizing constraint violations in the cost functional or by introducing additional Lagrange multipliers in the PMP formulation. In this work, hard enforcement through inequality checks during integration is adopted for simplicity.

Convergence and Numerical Considerations

The shooting—Newton approach typically converges quadratically when the initial guess is close to the true solution. However, nonlinearities in the dynamics and the discontinuous nature of the eclipse constraint can make the convergence sensitive. Common techniques to improve robustness include:

- Continuation methods: gradually varying problem parameters (e.g., thrust level or target conditions) to approach the final solution.
- Multiple shooting: splitting the integration interval into segments to improve numerical conditioning.
- **Hybrid approaches**: using a direct method to generate an initial guess for the indirect solver.

When implemented carefully, the indirect shooting approach provides highly accurate solutions and valuable analytical insight into the structure of the optimal control law, while remaining computationally efficient for problems of moderate dimension.

4.7 Graphical User Interface

The numerical tool employed in this work is based on *Oculus*, a graphical user interface originally developed by Mascolo [15] for solving low-thrust optimal control problems and visualizing the resulting orbital trajectories. Oculus provides a robust and modular environment that integrates trajectory optimization algorithms with a user-friendly interface, enabling intuitive interaction with the problem setup, solution, and visualization stages.

The software is structured around an indirect optimization framework and allows users to define initial and final orbital conditions, propulsion parameters, and integration settings. Once the problem is configured, the solver computes the optimal trajectory and displays its evolution both graphically and numerically, facilitating physical interpretation and analysis.

Building on this existing framework, the software used in this thesis has been significantly extended to address additional physical phenomena relevant to low Earth orbit missions. In particular, two major capabilities have been implemented:

- Atmospheric drag modeling: a module that computes atmospheric density using the NRLMSISE-00 model and evaluates drag acceleration. This required modifications to the equations of motion and the force model implemented in the solver.
- Eclipse constraint handling: a new functionality that determines when the spacecraft enters Earth's shadow based on solar ephemerides from SPICE kernels and enforces a thrust constraint that disables propulsion during eclipse phases.

These extensions required nontrivial changes to the dynamics propagation, costate integration, and Hamiltonian minimization procedures, while preserving the modular structure and interactive design of the original *Oculus* interface. As a result, the final software combines the versatility of the existing tool with new physical realism, enabling the simulation and optimization of low-thrust station-keeping trajectories under environmental constraints that were not originally supported.

Chapter 5

Result and Analysis

5.1 Simulation Setup and Parameters

To evaluate the performance of the optimal control strategies derived in the previous chapters, a set of numerical simulations was performed under different modeling assumptions. This section presents the simulation setup, including the orbital configuration, spacecraft characteristics, environmental models, and numerical parameters adopted throughout the analyses.

Orbital Configuration

The spacecraft is assumed to operate in a low Earth orbit (LEO), with parameters representative of typical small satellite missions. Unless otherwise specified, the nominal orbital elements at the initial epoch are:

- Semi-major axis: $a = R_{\oplus} + h_0$, with $h_0 = 300 \,\mathrm{km}$;
- Eccentricity: e = 0 (circular orbit);
- Inclination: $i = 96.5^{\circ}$ (sun-synchronous);
- Right ascension of ascending node: $\Omega = 0^{\circ}$;
- Argument of perigee: $\omega = 0^{\circ}$;
- True anomaly: $\nu = 0^{\circ}$.

These values correspond to a circular sun-synchronous orbit, a common choice for Earth observation and scientific satellites. The circular assumption simplifies the analysis while preserving the main dynamical effects relevant to the control problem.

Spacecraft Parameters

The simulated spacecraft properties are representative of a small satellite equipped with an electric propulsion system:

• Initial mass: $m_0 = 500 \,\mathrm{kg}$;

• Effective cross-sectional area: $A = 1 \,\mathrm{m}^2$;

• Drag coefficient: $C_D = 2.2$;

• Maximum thrust: $T_{\text{max}} = 0.5 \,\text{N}$;

• Specific impulse: $I_{sp} = 1000 \,\mathrm{s}$.

The thrust level and specific impulse are consistent with state-of-the-art electric propulsion systems for small satellites. The thrust is assumed constant in magnitude and aligned according to the optimal control law, when available power allows.

Environmental Models

Atmospheric drag is computed using the NRLMSISE-00 empirical model implemented via the pymsis library [10]. This model accounts for the effects of solar and geomagnetic activity through the $F_{10.7}$ solar flux and A_p geomagnetic index. The baseline simulations use:

$$F_{10.7} = 150, \qquad A_p = 10.$$

Solar position is obtained from NAIF SPICE ephemerides [14], ensuring accurate Sun vector computation in the ECI frame. Eclipse detection is performed using the conical shadow model described in Section 4.4. Thrust is set to zero whenever the illumination function satisfies $\chi_{\text{sun}}(t) = 0$.

Numerical Solver and Integration Settings

The coupled state—costate equations are integrated using a variable-step, adaptive Runge—Kutta 4(5) method (Dormand—Prince, RK45). A relative tolerance of 10^{-10} and an absolute tolerance of 10^{-12} are used to ensure numerical accuracy. Event detection is implemented to precisely locate eclipse entry and exit points by monitoring the sign of the shadow boundary functions.

The total integration time spans T=7 orbital periods, sufficient to capture multiple eclipse cycles and evaluate the long-term impact of drag and thrust scheduling. The indirect shooting method combined with Newton iteration is employed to solve the resulting TPBVP, as described in Section 4.6.

Simulation Cases

To systematically assess the influence of drag and eclipse constraints, three main simulation cases are considered:

- 1. Case A Ideal dynamics: only two-body gravitational acceleration and continuous thrust are included (no drag, no eclipse).
- 2. Case B Atmospheric drag: drag is included, but the eclipse constraint is neglected ($\chi_{\text{sun}}(t) = 1$).
- 3. Case C Full model: both drag and eclipse constraints are included.

This progressive approach isolates the effect of each physical phenomenon and highlights its impact on the optimal solution.

5.2 Baseline Case – Ideal Dynamics (No Perturbations)

As a reference scenario, the optimal control problem was first solved assuming an ideal two-body environment without atmospheric drag or eclipse constraints. In this case, the spacecraft is subject only to Earth's central gravitational attraction and a continuous low-thrust acceleration with constant magnitude $T_{\rm max}$. The thrust direction is optimized according to the Pontryagin Minimum Principle described in Chapter 4.5.

Problem definition

The objective of this case study is to determine the optimal low-thrust control profile required to raise the satellite's orbit from an initial circular altitude of 300 km to a final altitude of 302 km. This manoeuvre is designed as a representative station-keeping operation in Low Earth Orbit (LEO), where atmospheric drag continuously reduces the spacecraft's orbital energy and causes a gradual decay of the semi-major axis.

Although the atmospheric drag effect is not explicitly included in this first scenario, the two-kilometre altitude increase anticipates the counteraction of this perturbation and ensures that the satellite remains close to its nominal operational orbit over time. The manoeuvre is performed using continuous low-thrust propulsion aligned with the direction of motion, and the optimization is aimed at minimising the propellant consumption required to achieve the desired orbital raise.

Since no environmental perturbations are present, the control is free to operate continuously, and the illumination function is identically $\chi_{\text{sun}}(t) = 1$.

Numerical Results

The baseline simulation demonstrates the expected characteristics of low-thrust motion in an unperturbed environment:

- Orbital evolution: the altitude increases smoothly with no oscillations, as the thrust is continuously aligned with the velocity vector.
- Mass variation: the propellant mass decreases linearly with time due to the constant thrust magnitude when T = Tmax.
- Thrust profile: thrust is active at the start of the orbit, in the middle and in the end.

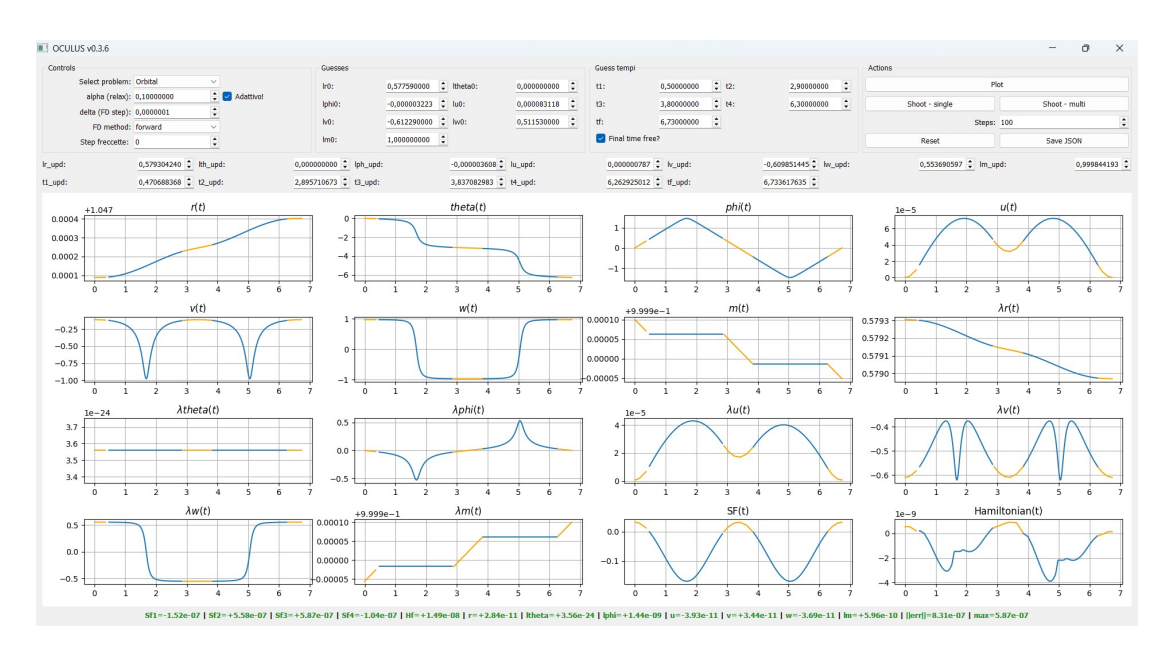


Figure 5.1: Baseline case: Variable evolution under low thrust in a two-body environment.

The baseline solution provides a reference for quantifying the effects of environmental perturbations. In particular, it highlights the efficiency of the thrust system in an idealized scenario and serves as a benchmark for evaluating the additional control effort required when drag and eclipse constraints are introduced.

Discussion

The results of the baseline case show that the optimal control solution does not consist of a continuous thrust profile over the entire transfer, as might be expected

from a purely analytical perspective. Instead, the thrust is applied in a series of distinct arcs separated by coast phases in which the engine is turned off.

Specifically, the solution exhibits five distinct phases: an initial thrust arc that accelerates the spacecraft and begins to raise the orbit, followed by a coast phase during which the orbital motion evolves naturally under gravity. This is then followed by a second thrust arc, a second coast phase, and a final thrust arc that completes the transfer to the target altitude.

This structure arises from the optimisation process itself and reflects the interplay between thrust direction, mass variation, and the nonlinear orbital dynamics. By concentrating thrust into discrete arcs rather than spreading it continuously, the solution minimises propellant consumption while still achieving the required change in orbital energy.

Such bang-bang-like structures are well known in optimal low-thrust control problems [11, 13], even when no explicit constraints on thrust availability are imposed. The presence of coast phases is therefore not a numerical artifact, but an intrinsic feature of the optimal solution.

5.3 Dynamics with Atmospheric Drag Only

Problem description

In this second scenario, the effect of atmospheric drag is included in the dynamical model, while the eclipse constraint remains inactive ($\chi_{\text{sun}}(t) = 1$). All other parameters, including thrust magnitude, specific impulse, and initial and final orbital conditions, are the same as in the baseline case. The objective remains to raise the spacecraft's altitude from 300 km to 302 km, compensating for the energy loss caused by drag.

Results and Discussion

The inclusion of atmospheric drag does not qualitatively change the structure of the optimal thrust profile: the solution still consists of multiple thrust arcs separated by coast phases, as already observed in the baseline case. The main difference lies in the **increased duration of the thrust phases**, which reflects the need to compensate for the continuous loss of orbital energy caused by drag.

The optimisation naturally responds to this perturbation by increasing the total impulse delivered along the orbit, without altering the fundamental thrust—coast—thrust structure. As a result, the overall transfer takes slightly longer and the propellant consumption is higher compared to the drag-free scenario.

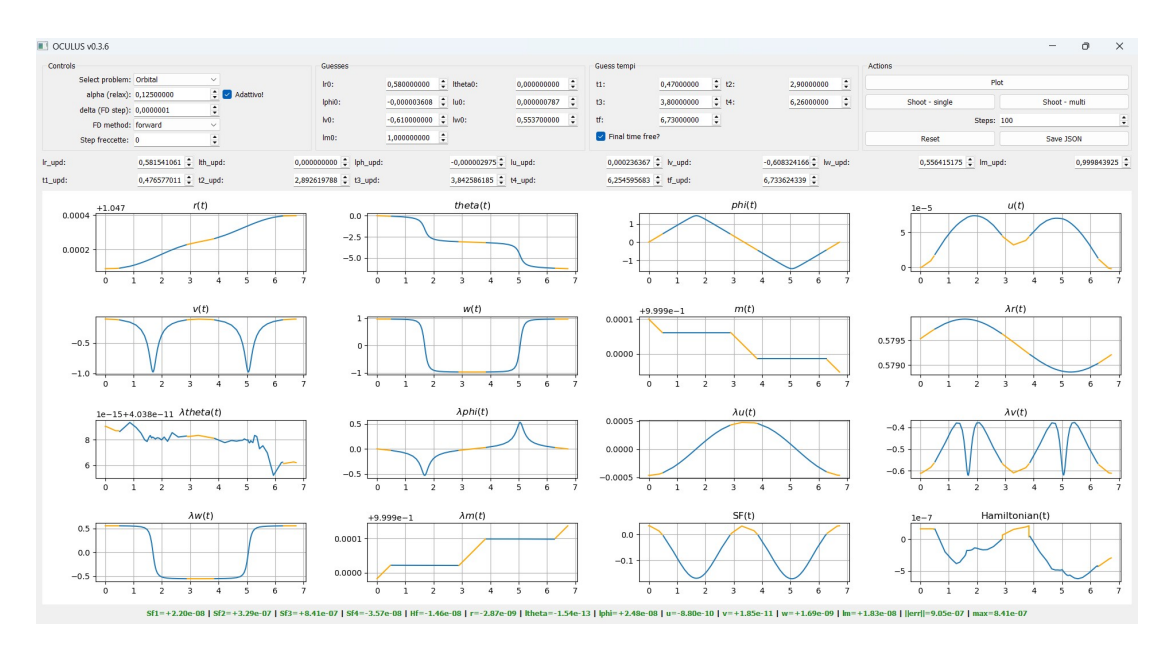


Figure 5.2: Time evolution of the state variables for the drag-included scenario.

The figure above shows the time evolution of the main state variables. Despite the presence of drag, the system follows a trajectory qualitatively similar to the baseline case, with the increased thrust duration clearly visible in the orbital evolution. This demonstrates how atmospheric drag, though relatively weak at these altitudes, has a measurable impact on the control strategy and mission timeline.

5.4 Full Model: Drag and Eclipse Constraint

Problem Description

The third and final scenario incorporates both atmospheric drag and the eclipse constraint into the optimal control formulation. As before, the objective is to raise the spacecraft's altitude from 300 km to 302 km using low-thrust propulsion, while minimising propellant consumption. The eclipse constraint is implemented by enforcing $\chi_{\text{sun}}(t) = 0$ when the spacecraft is in Earth's shadow, thereby preventing thrusting during eclipse phases.

This case represents the most realistic operational condition, as it combines the primary environmental perturbation in low Earth orbit with the power-generation limitations imposed by solar illumination. The solution therefore provides insight into the control strategy required for station-keeping in a practical mission context.

Orbital Evolution and Thrusting Pattern

The inclusion of the eclipse constraint significantly influences the optimal control profile without altering the overall mission objective. The total altitude increase remains essentially the same as in the previous scenarios, but the temporal distribution of thrust is markedly different.

In the baseline and drag-only cases, thrust was applied in several distinct arcs distributed across the orbit. In contrast, the presence of eclipse windows now prevents thrusting during certain orbital phases. As a result, the optimiser shifts the control effort toward periods of continuous solar illumination, leading to longer thrust arcs concentrated at the beginning and end of the manoeuvre, and shorter thrust segments — or complete coast phases — in the central portion of the trajectory.

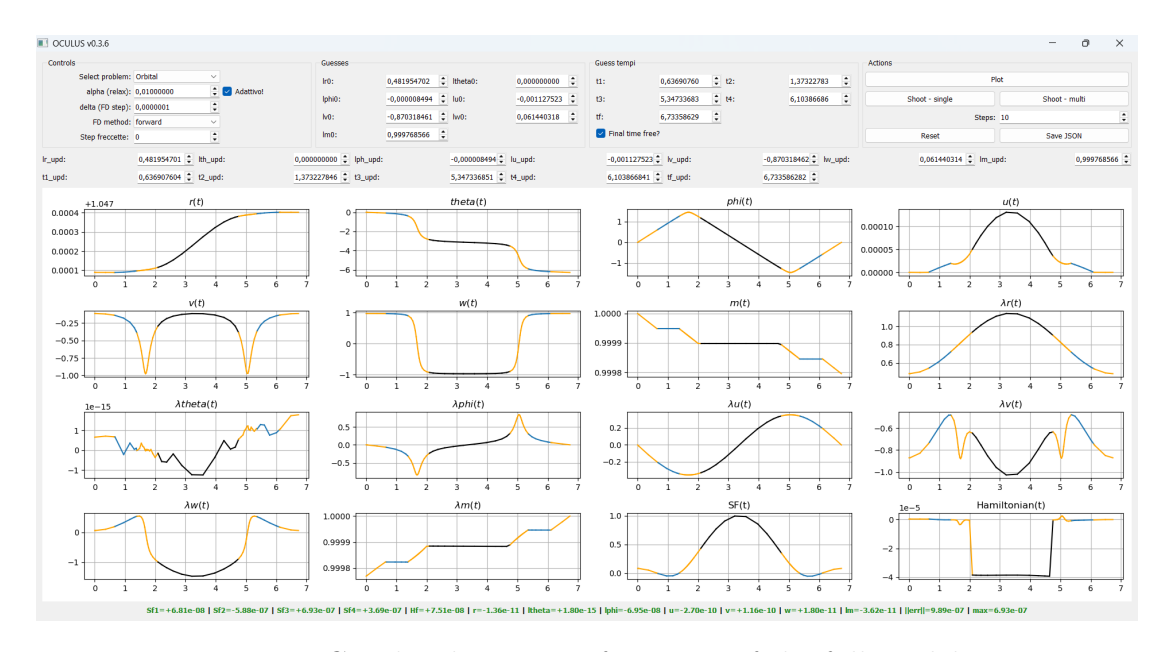


Figure 5.3: Graphical user interface view of the full-model case.

The time history of the state variables shows that the altitude raise is still achieved within the mission requirements, but the profile reflects the constrained thrust availability. In particular, the radial velocity component exhibits longer periods of acceleration early and late in the transfer, corresponding to the extended thrust phases outside of eclipse.

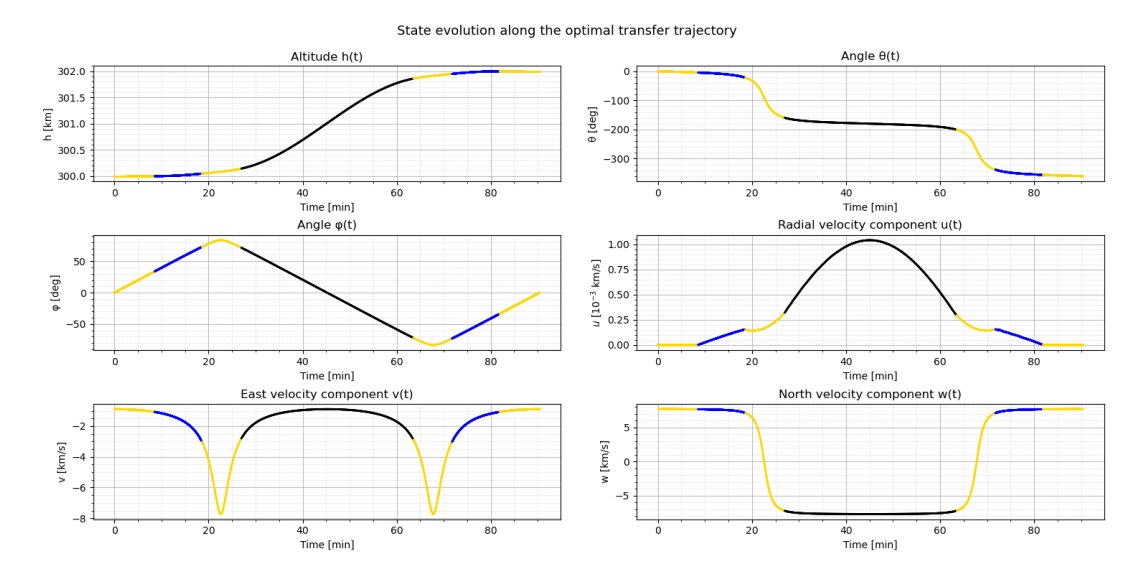


Figure 5.4: Time evolution of the state variables for the full-model case.

Physical Interpretation and Implications

This final scenario highlights the critical impact of environmental constraints on the structure of optimal control solutions. Even though the total Δh is unchanged, the necessity to interrupt thrust during eclipse phases leads to a redistribution of control effort. The spacecraft compensates for the unavailable thrust periods by increasing the duration and intensity of thrusting before and after the shadow interval.

This behaviour has important implications for mission design. It suggests that, when eclipse windows are present, thrust planning cannot rely solely on idealised continuous-control assumptions. Instead, the mission timeline, power availability, and control law must be designed together to ensure that sufficient thrust can be delivered during illuminated arcs. The resulting strategy preserves propellant efficiency while respecting the physical limitations imposed by the space environment.

Chapter 6

Conclusions and Future Work

Conclusions

This thesis presented the formulation, numerical solution, and analysis of an optimal control problem for low-thrust satellite operations in Low Earth Orbit (LEO), with particular emphasis on the effects of atmospheric drag and eclipse constraints. The work combined high-fidelity dynamical modeling, indirect optimal control techniques, and numerical implementation in a dedicated Python environment with a graphical user interface.

The main contributions and findings can be summarized as follows:

- A comprehensive dynamical model was developed in spherical coordinates, including central gravitational attraction, atmospheric drag based on the NRLMSISE-00 density model, and the time-dependent illumination function derived from cylindrical shadow geometry. This model captures the key environmental effects relevant to low-thrust LEO missions.
- The optimal control problem was formulated using Pontryagin's Minimum Principle, leading to a two-point boundary value problem solved through an indirect shooting method combined with Newton iteration. This approach provided high-accuracy solutions and clear insight into the structure of the optimal control law.
- A detailed analysis of the effects of drag and eclipse on the optimal solution revealed their significant impact on mission performance. Drag continuously reduces orbital energy and requires additional thrust to maintain altitude, while

eclipse intervals impose strict constraints on thrust availability, introducing discontinuities in the control profile and reducing overall acceleration.

- A progressive set of simulations from an ideal two-body case to a full model including both drag and eclipse — demonstrated how each physical effect modifies the optimal solution. The comparison showed that neglecting these effects can lead to substantial underestimation of propellant use and mission duration.
- A modular software tool was developed to implement the model and optimization algorithm, providing a flexible framework for scenario definition, simulation, and visualization. The inclusion of a graphical user interface enhances usability and supports rapid parametric studies.

Overall, the results demonstrate that accounting for both atmospheric drag and eclipse constraints is essential in the design of realistic low-thrust stationkeeping and orbit maintenance strategies. These effects significantly influence the structure of the optimal control law, the propellant budget, and the achievable orbital performance. The methodology developed in this work provides a rigorous foundation for preliminary mission analysis and can be extended to support future operational planning.

Future Work

Several extensions of this work are possible and represent valuable directions for future research:

- Inclusion of higher-order gravitational effects: Incorporating Earth's oblateness (J_2) and higher-order harmonics would allow the framework to be applied to long-term station-keeping and ground-track repeat missions.
- Inclusion of additional perturbations: Modeling solar radiation pressure and third-body effects would further improve fidelity, particularly for higher orbits or extended mission durations.
- Robust and adaptive control strategies: Extending the framework to include robust or feedback-based control laws could improve performance under uncertainty, such as variable atmospheric density or thrust fluctuations.
- **Direct optimization approaches:** Implementing direct transcription or collocation methods would enable the solution of more complex problems, such as multi-phase maneuvers, minimum-time transfers, or missions with additional constraints.

• Hardware-in-the-loop validation: Coupling the software with hardware simulators or propulsion system testbeds would support experimental validation and accelerate the transition to operational applications.

In conclusion, this work provides both a theoretical and practical foundation for the optimal control of low-thrust spacecraft in LEO. By integrating accurate environmental modeling with indirect optimization techniques, it contributes to the development of more efficient and realistic station-keeping strategies. The results and methodologies presented here are not only relevant for small satellite missions but can also be extended to future distributed space systems, Earth observation constellations, and scientific platforms requiring precise orbital control under challenging environmental conditions.

Bibliography

- [1] Luigi Mascolo. «Low-Thrust Optimal Escape Trajectories from Lagrangian Points and Quasi-Periodic Orbits in a High-Fidelity Model». PhD thesis. Politecnico di Torino, 2019 (cit. on pp. 4, 11, 12, 14, 16, 19, 24, 26, 27, 29, 31).
- [2] David A. Vallado. Fundamentals of Astrodynamics and Applications. 4th. Microcosm Press, 2013 (cit. on pp. 11–13, 15–17, 20, 40, 42).
- [3] Manuela Battipede. Mechanics of Space Flight Lecture Slides (1–11). Slides on Two-Body Problem, Reference Frames, Perturbations, Orbital Transfers, and Three-Body Problem. 2023 (cit. on pp. 13, 15–18, 20).
- [4] Richard H. Battin. An Introduction to the Mathematics and Methods of Astrodynamics. Revised. AIAA Education Series, 1999 (cit. on pp. 13, 16, 17).
- [5] Giuseppe Carone. «LEO Satellite Dynamics and Low-Thrust Optimization under Drag and J2 Perturbations». MA thesis. Politecnico di Torino, 2023 (cit. on pp. 14, 16–19).
- [6] Giuseppe La Barbuta. «Low-Thrust Optimal Control of Orbital Trajectories with Eclipse Constraints». MA thesis. Politecnico di Torino, 2021 (cit. on pp. 14, 19).
- [7] Giuseppe Francesco Marinelli. «Trajectory Optimization for Space Debris Removal using Indirect Methods». MA thesis. Politecnico di Torino, 2025 (cit. on p. 16).
- [8] Nicola De Bari. «Analysis of Sun-Synchronous Orbits and Perturbative Models for Earth Observation Satellites». MA thesis. Politecnico di Torino, 2024 (cit. on pp. 16–18).
- [9] NASA Goddard Space Flight Center. J2 Perturbation Model and Nodal Precession Derivation. https://gssc.esa.int/navipedia/index.php/J2_Perturbation. 2021 (cit. on p. 17).
- [10] Michael Hirsch et al. PyMSIS-00: Python Interface for the NRLMSISE-00 Atmospheric Model. https://github.com/space-physics/pymsis. 2020 (cit. on pp. 19, 38, 50).

- [11] Arthur E. Bryson and Yu-Chi Ho. Applied Optimal Control: Optimization, Estimation and Control. Taylor & Francis, 1975 (cit. on pp. 24, 26, 27, 29, 31, 33, 53).
- [12] Donald E. Kirk. *Optimal Control Theory: An Introduction*. Dover Publications, 1970 (cit. on pp. 24, 26, 27, 29, 31, 33).
- [13] Lev S. Pontryagin, Vladimir G. Boltyanskii, Revaz V. Gamkrelidze, and Evgenii F. Mishchenko. *The Mathematical Theory of Optimal Processes*. New York: Interscience Publishers (John Wiley & Sons), 1962 (cit. on pp. 24, 27, 53).
- [14] NASA Navigation and Ancillary Information Facility (NAIF). SPICE Toolkit. https://naif.jpl.nasa.gov/naif/. 2022 (cit. on pp. 40, 42, 50).
- [15] Luigi Mascolo. «OCULUS A Unified Visual Solver for Optimal Control Problems via Indirect Methods». In: *Proceedings of the 76th International Astronautical Congress (IAC)*. Paper IAC–25–E1.4.4.x103041. International Astronautical Federation (IAF). Sydney, Australia, Sept. 2025. URL: https://iris.polito.it/handle/11583/2976595 (cit. on p. 48).
- [16] Luca Nitti. «Indirect Optimization of Low-Thrust Trajectories in the Circular Restricted Three-Body Problem». MA thesis. Politecnico di Torino, 2024.
- [17] Andrea Pice. «Trajectory Optimization in Multi-Body Dynamical Systems via Indirect Methods». MA thesis. Politecnico di Torino, 2024.
- [18] Federico Sarcletti. «Indirect Optimal Control for Low-Thrust Transfers in the Earth–Moon System». MA thesis. Politecnico di Torino, 2024.
- [19] Edoardo Bruno. «Low-Thrust Mission Design for Asteroid Rendezvous within the Earth–Sun System». MA thesis. Politecnico di Torino, 2024.
- [20] D.D. McCarthy and G. Petit. *IERS Conventions* (2010). https://iers-conventions.obspm.fr. 2010.
- [21] International Astronomical Union. IAU SOFA (Standards of Fundamental Astronomy) Software Collection. https://www.iausofa.org. 2022.
- [22] John E. Prussing and Bruce A. Conway. *Orbital Mechanics*. 2nd. Oxford University Press, 2013.
- [23] Hanspeter Schaub and John L. Junkins. *Analytical Mechanics of Space Systems*. 3rd. AIAA Education Series, 2015.
- [24] NASA Jet Propulsion Laboratory. Patched-Conic Approximation and Sphere of Influence. https://ssd.jpl.nasa.gov. 2020.